Modeling of a High Charge Injector for the TESLA Test Facility

B.M. DUNHAM and M. JABLONKA
DAPNIA/SEA, CE Saclay, 91191 Gif/Yvette

February 25, 1994

Abstract

Several possible models for a high charge injector for the Tesla Test Facility have been studied. The injector is required to produce 5×10^{10} e^-/bunch with a pulse length of $\sigma_z = 1$ mm at a repetition rate of 1 MHz during a macropulse length of 800 μs and a duty cycle of 1%. An injection scheme using only superconducting cavities would not work because solenoidal focusing cannot be provided along the length of the structure to compensate for the high space charge forces. It is demonstrated that a short, normal conducting buncher operating at ~5 MV/m can efficiently preaccelerate the beam. It is then accelerated through a 9-cell SC capture cavity and compressed to the required bunch length using a chicane-type magnetic buncher. Two possible schemes are discussed, one starting with a 250 kV thermionic gun, and a second starting with a 500 kV DC photocathode gun. The thermionic case requires initial bunching using two subharmonic cavities, while the photocathode gun solution does not. Simulations of the entire injector for both cases show that the needed bunch length can be obtained with a final emittance of ~50 π mm mrad (normalized, rms). Also discussed are some of the features and problems with using the PARMELA space charge routines.

Contents

1 Introduction

A high charge injector (injector #2) for the Tesla Test Facility (TTF) is required for testing the superconducting (SC) accelerating structures under the planned operating conditions of the TESLA linac. The injector must produce not only very high charge bunches (5×10^{10} e$^-$), but also very short bunches (σ_z = 1 mm, or 1.6° of RF phase).

A number of high charge injectors similar to that needed for TTF are already in existence or in the planning stages (see table 1). These in-

Lab	freq (MHz)	SHB (MHz)	Q (nC)	$\epsilon_{n,rms}$ (π mm-mrad)	τ_{FWHM} (ps)	I_{peak} (A)	ref
Argonne	1300	108	10	310	25	400	[1]
SLC	2856	178,178	8	150	20	400	[2]
Boeing	1300	108,433	3.5	15	12	290	[3]
Osaka	1300	108,433	10	60	16	600	[4]
NLC*	1428	714,714	8	22	16	500	[5]
TTF*	1300	?	8	80	5	1600	

Table 1: Parameters of some existing high charge injectors (* design value).

jectors have a number of features in common: they utilize 100–250 kV thermionic electron guns; one or more subharmonic bunching cavities; a traveling wave (TW) capture section; and solenoidal focusing all along the beamline. Direct application of one of these injectors for the TTF injector would be difficult, though, as TTF requires a macropulse length nearly 1000 times longer, and with a much higher duty cycle (1%). In particular, the new design for the TW section that would be needed to accomodate the higher average RF power is certainly a difficult task. One aspect of the design of the TTF injector is to use conventional, readily available components whenever possible. By doing this one hopes, of course, to save money and to complete the injector as quickly as possible. Thus components like a TW capture section capable of high power dissipation, or an RF gun (under study by other members of the TESLA collaboration) were not considered.

This report will investigate several models that meet the requirements of a high charge injector for the TTF. Simulations using PARMELA [6] are presented, and the use of PARMELA is discussed.

2 Magnetic Bunchers

In order to reach the desired bunch length of 1 mm, it has been found necessary to perform magnetic bunching after the RF bunching process in all of the models studied. For TESLA, this magnetic compression will be

carried out at very high energy where space charge is not a problem. For TTF, however, this is not possible, and the beam must be compressed at low energy before injection into the main linac.

There are two types of magnetic bunchers (MB) typically used for low energy beams, a chicane-type (with negative dispersion) and a circular-type (with positive dispersion) (see [7] and figure 1). The circular buncher has

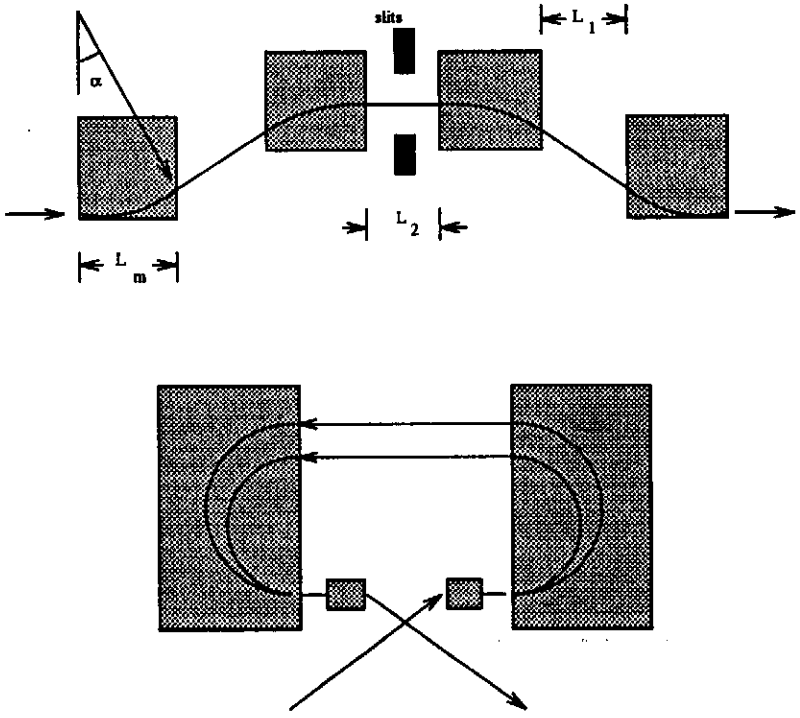

Figure 1: A chicane-type magnetic buncher (top) and a circular-type magnetic buncher (bottom).

the advantage of having a dispersion which is linear with momentum and it has a greater dispersion than for the chicane-type for the same path length. For the chicane-type buncher, the dispersion depends on the momentum through the sine of the bend angle of the first magnet and the non-linearities introduced are undesirable from the point of view of emittance growth. From a design point of view, though, the chicane buncher is probably simpler, requiring only four identical rectangular bending magnets. As it turns out, for the models under investigation, the size and magnetic field necessary for a circular buncher with the appropriate path length variation are not easily realizable and are not considered further.

The transverse optical properties of a chicane-type magnet buncher consisting of four identical, rectangular magnets is quite simple. For a bend angle of 30°, magnet length L_m = 15 cm, and drift spaces L_1 = 7 cm and L_2 = 0 cm (refer to figure 1) the first order transfer matrix (units are cm

and mrad) is

$$\mathbf{R} = \begin{pmatrix} 1. & .085 & 0 & 0 & 0 & 0 \\ 0 & 1. & 0 & 0 & 0 & 0 \\ 0 & 0 & -.82 & .014 & 0 & 0 \\ 0 & 0 & -22.2 & -.82 & 0 & 0 \\ 0 & 0 & 0 & 0 & 1 & .108 \\ 0 & 0 & 0 & 0 & 0 & 1 \end{pmatrix}. \tag{1}$$

In the bend plane, the matrix is equivalent to a drift space, while the non-bend plane is equivalent to a thick focusing lens. The R_{56} matrix element (0.108 cm/%) gives the path length difference for particles of varying momentum. The buncher also has a several higher order terms which are significant,

$$\begin{array}{lll} T_{133} = -.03 & T_{323} = 0.003 & T_{424} = -.003 \\ T_{134} = -.002 & T_{336} = 0.02 & T_{436} = -.7 \\ T_{144} = -.0002 & T_{346} = 0.001 & T_{446} = 0.02 \\ T_{126} = -.0004 & & T_{566} = -.002. \end{array} \tag{2}$$

It will be shown later that emittance growth due to these aberrations is negligible under certain conditions (see section 3.3).

In longitudinal phase space, the magnetic buncher works by providing a longer path for particles at the head of the bunch (lower energy) relative to those at the tail of the bunch (higher energy) to allow the particles at the tail to catch up. This is accomplished by imparting an appropriate energy variation along the bunch by adjusting the phase in a RF buncher or accelerating cavity. If a bunch has an intrinisic energy spread $\sqrt{\sigma_{66}^{\text{intrinsic}}}$, an initial bunch length $\sqrt{\sigma_{55}^{\text{init}}}$, and a phase-energy tilt f_{56}, then the final bunch length after compression is given by [8]

$$\begin{aligned} \sigma_{55}^{\text{final}} &= \sigma_{55}^{\text{init}}(1 - R_{56}/f_{56})^2 + R_{56}^2\sigma_{66}^{\text{intrinsic}} \\ f_{56} &= -\sigma_{55}^{\text{init}}/\sigma_{56}^{\text{init}}. \end{aligned} \tag{3}$$

If R_{56} is set equal to the phase-energy slope f_{56}, then it is found that the final bunch length is minimized and depends only on R_{56} and the initial intrinsic energy spread of the beam. PARMELA has been modified to print out the number f_{56} to aid in designing the chicane. After performing a PARMELA run up to the point where the magnetic buncher will start, the calculated f_{56} value is used as a constraint in TRANSPORT to adjust the drift length (L1) and bend angle (α) of the chicane. Then PARMELA is run again using the matched chicane.

3 PARMELA and Space Charge Calculations

3.1 General Considerations

PARMELA has been in use for many years and its general acceptance is evidenced by the many references to it in journals and conferences. There are a number of problems in using the program, though. First, many different versions exist which make comparisons with other results from laboratories difficult. Second, the available documentation is very sparse, undoubtly causing many people to spend time developing subroutines that have been written many times before. Finally, it is not at always clear that the obtained results are believable: they can vary dramatically depending on the input parameters, especially with the space charge routine. For example, in table 1 the measured results at the SLC of 150 π mm-mrad (normalized, rms) are nearly double the PARMELA results of 80 π mm-mrad [2], while the measured Boeing results of 15 π mm-mrad are less than the PARMELA results of 50 π mm-mrad [3].

Another problem that arises is that in the literature, people often mention only the results of simulations and nothing about how they got those results. This makes it very difficult to use the work of other groups, which is very important in a study such as this in which we are trying not to waste time and money by reinventing the wheel. So, the remainder of this section will include a discussion of the parameters used in these PARMELA simulations, mainly those of the space charge routines which cause the greatest variations in the output.

There are two methods for calculating the space charge forces on the macroparticles in PARMELA (see [9] for a recent reference). The first involves superimposing a 2-D, cylindrically symmetric mesh over the particle distribution in the rest frame of the bunch and calculating the fields due to the particles in the bins. The mesh method has the advantage of running quickly which is advantageous for optimization, but there are many free parameters to set. One has to provide the physical dimensions of the mesh (r_{mesh}, z_{mesh}), the number of bins (N_r, N_z), and a form factor for taking acceleration into account, for example. The second method is a 3-D, point-to-point calculation [10] in which the forces between macroparticles are calculated directly. This method is very slow compared to the mesh method, but there is only one free parameter, a screening factor to insure that the forces are not overestimated for overlapping macroparticles.

For investigating various models, the mesh calculation is used to optimize the injector characteristics, and the point-to-point calculation is used only as a check on the results. In our experience, the point-to-point method predicts a larger emittance than for the mesh method. The difference grows larger as the phase space becomes non-cylindrically symmetric or becomes distorted due the bunching process.

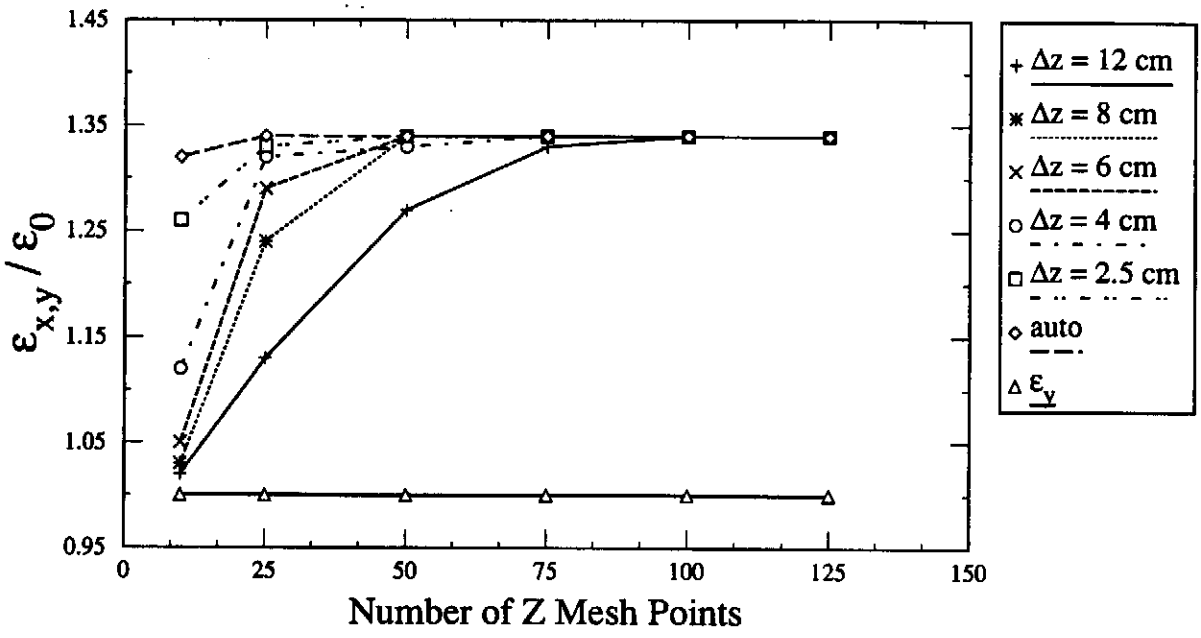

Figure 2: The emittance growth in a magnetic buncher for various PARMELA space charge parameters.

3.2 Emittance and the Mesh Method

As there are many free parameters for the mesh calculation, it is necessary to investigate parameter space to verify that the results converge. The calculated final emittance varies more drastically than other physical quantities of interest, so that is the quantity to be used for comparisons here. A magnetic buncher (as described in section 2) is used as a test case. The input phase space is an idealization of the phase space at the output of the original model used for injector #2 [11]. The longitudinal phase space is an ellipse with $f_{56} = .108$, and an average energy of 7 MeV. The transverse phase space is an upright ellipse with an initial beam radius of 4 mm and an emittance of 300 π mm-mrad (all emittances from here on are normalized and 4 $\times$ the rms value unless otherwise noted). The beam charge is 8 nC divided amongst 1000 macroparticles. The PARMELA input deck is shown in Appendix A.

In figure 2, the emittance growth through the MB is displayed as a function of the number of bins (N_z) used in the mesh along the beam direction. Each curve shows the result for a different mesh length (z_{mesh}). The number of bins and mesh length along the radial direction are not varied ($N_r = 30$, $r_{mesh} = 1.8$ cm). As the bunch becomes non-symmetric as it passes through the buncher, a built-in feature mapping the elliptical transverse beam distribution onto a cylindrically symmetric distribution is invoked. The emittance

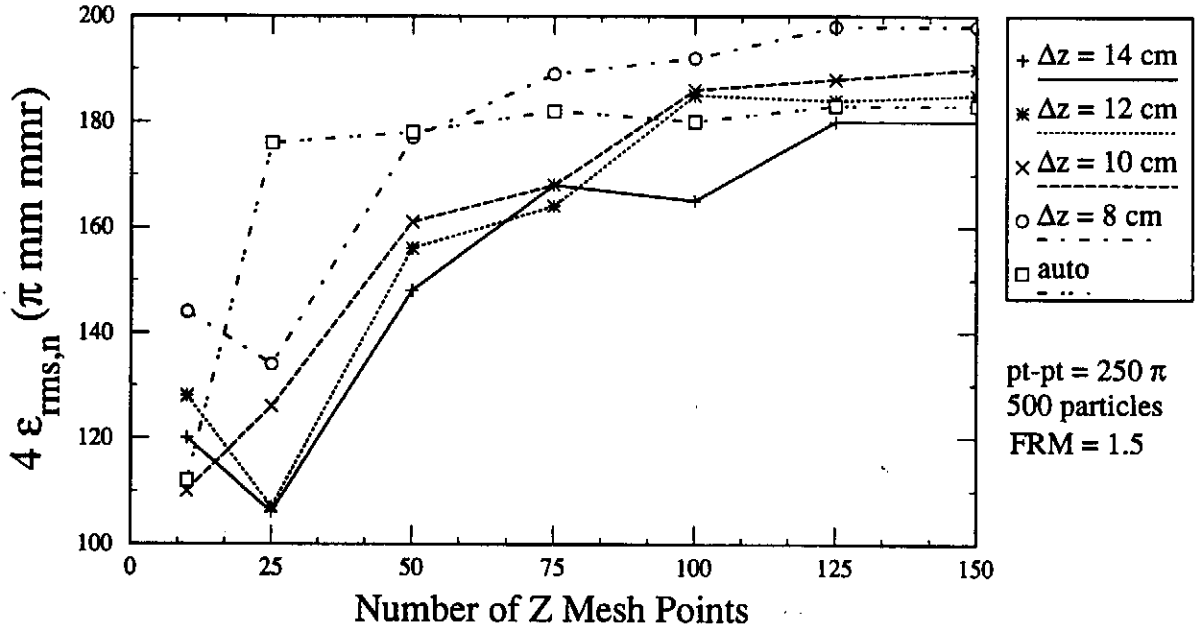

Figure 3: The final emittance for the injector model for various PARMELA space charge parameters.

growth in the non-bend plane as seen on the figure is negligible, as expected. For the initial run, 25 bins with a mesh length of 12 cm was chosen. The mesh length was erroneously chosen to be more than three times longer than the actual bunch length, and the predicted emittance growth was very small. By increasing the number of bins, the emittance eventually reaches a constant value. As the initial mesh length is decreased, the constant value is obtained using fewer bins. This points out that it is easy to make drastic errors with a poor choice of parameters. The best case is shown by the curve labelled 'auto'. Here the bunch length is calculated and the mesh size is reduced every time the bunch length decreases by a given factor (1.5 in this example) using a subroutine developed by us. The final emittance converges to a constant value with the least number of bins. This is important to know when optimizing a beamline so as to be able to use the fewest bins possible to obtain consistent results in the least amount of time. This adaptive longitudinal mesh routine is used for the remainder of the calculations described in this report.

Consider another example in which the emittance growth as a function of the number of bins (N_z) and the mesh length (z_{mesh}) is plotted (see figure 3), this time using an injector consisting of a gun, subharmonic bunchers, and a RF buncher as a model (see section 4.3 for details). The 'auto' method again gives the fastest convergence, but this time there is a range of final values (depending on the initial mesh size) instead of a single value. It is

postulated that this is caused by the much greater distortion of the phase space due to the passage through several RF cavities, which were not present in the MB model used above. The point-to-point method predicts a value of 250 π mm-mrad (screening factor of 1.75), nearly 50% higher than for the mesh method.

In conclusion, it is necessary to be very careful in choosing the parameters when using the mesh space charge calculation method. A study of the parameter space yields a range of values which give consistent (but not necessarily correct) results.

3.3 Other Considerations for Magnetic Bunchers

In figure 4, the emittance growth through the MB is shown, but this time the

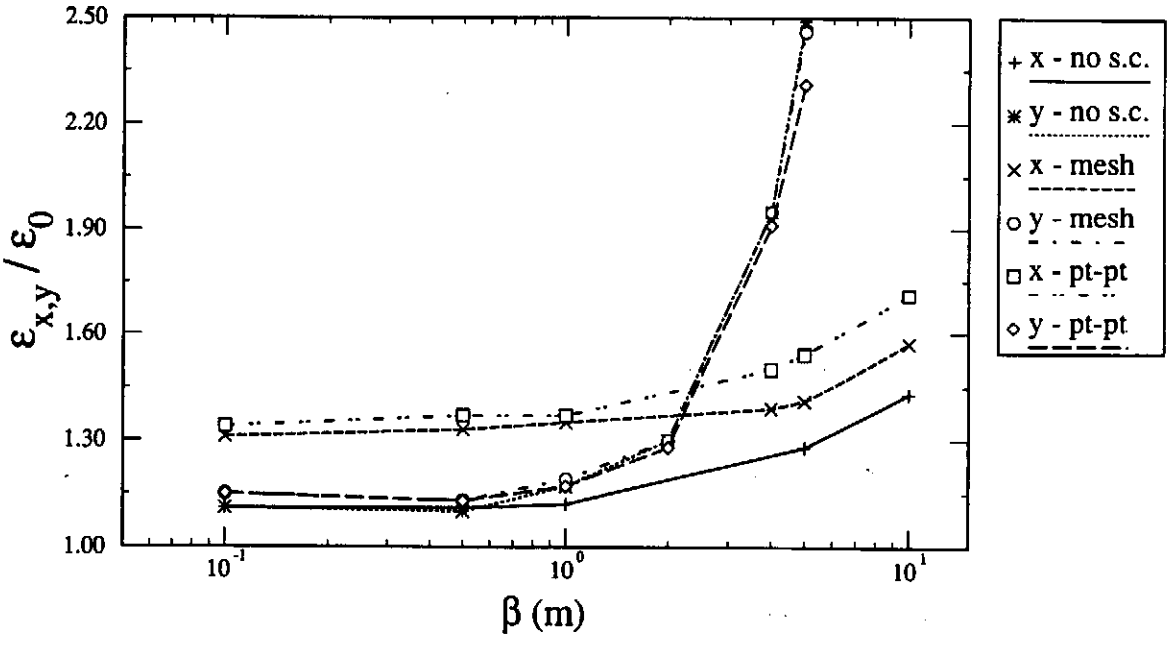

Figure 4: The emittance growth as a function of β in a magnetic buncher.

size of the beam at the entrance (the β function) is varied while the number of bins is held constant (N_z = 30) and the 'auto' method is used. The different curves show results for the cases of: the space-charge calculation turned off; using the mesh method; and using the point-to-point method. For the non-bend plane, where space charge is not a problem, all three calculation give approximately the same result. The large enhancement of the emittance with increasing β is due, in this case, to the aberrations of the system and not due to space charge. So one can see that by keeping β small enough the aberrations do not affect the emittance and complicated optical correction schemes can be avoided. The aberrations in the bend plane are

less important, but the calculations give different results due to the space charge. The point-to-point method estimates more growth than does the mesh method, as is usually the case for the studies performed here.

3.4 Parmela components

Before describing several alternative solutions for injector #2, the realization of the physical elements used in PARMELA will be given. For simplification sake, hard edge solenoids are used to model the magnetic field along the beamline. The use of hard edge solenoids is only an approximation but it makes the job of optimization of the injector much easier as it is trivial to change the field values.

The subharmonic bunchers are simulated using a zero-length, ideal buncher with a sinusoidal field. Studies have shown that there is very little difference between the use of a zero-length subharmonic buncher, and one described by actual field values.

The normal-conducting buncher is described using the internal field values provided in PARMELA. There are two types of structures available at 1300 MHz: a Chalk River on-axis coupled structure; and a Los Alamos side-coupled structure. Both types have been used as models. In addition, a constant, external magnetic field can be included over the length of the cell.

The fields of the 9-cell SC cavity have been reproduced with a method similar to that used at CEBAF. The axial field of the cavity is calculated using URMEL along a distance of 1.3 m, thus including the fringe field region (see fig 5). A complex Fourier transform is performed and the data is included in a subroutine (see Appendix B) which can reconstruct the electric and magnetic fields in the cavity. A new element (called 'cel9t') is defined and is called with the following parameters: aperture dimension; print control; phase; peak field; cell number; and step size. See Appendices C and D for examples.

4 Injector Models

4.1 Introduction

A brief description of the low charge injector [12] (injector #1) for TTF is in order as it is desirable to utilize the existing hardware and available space as best as possible. Injector #1 (see figure 6) begins with a 40 kV thermionic electron gun and an accelerating column to produce a beam of 250 keV. It is followed by a subharmonic cavity to bunch the beam before injection into a 9-cell SC capture cavity. After passing through the SC cavity, the beam traverses a $\sim$ 5 m beam analysis section before entering the main linac.

This electron gun-column is not suitable for injector #2 due to the difficulty of transporting a high charge through the column while maintaining a good emittance. Obtaining a gun with a total voltage of at least 250 kV

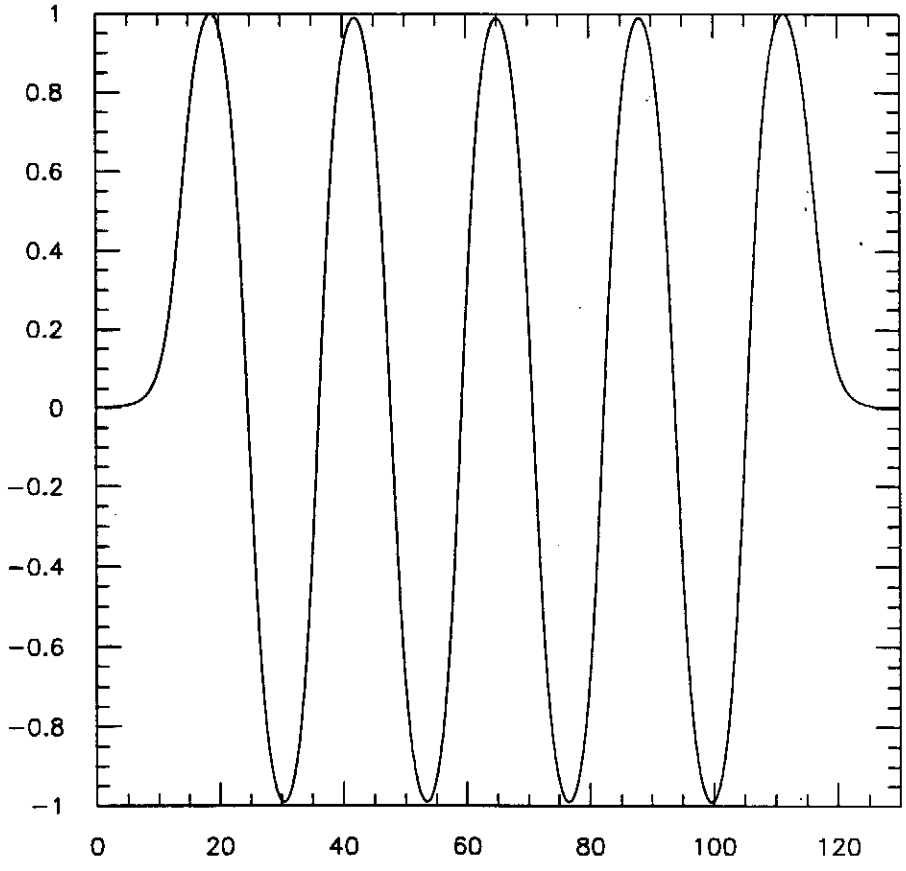

Figure 5: The normalized electric field along the axis (in cm) of the 9-cell SC cavity.

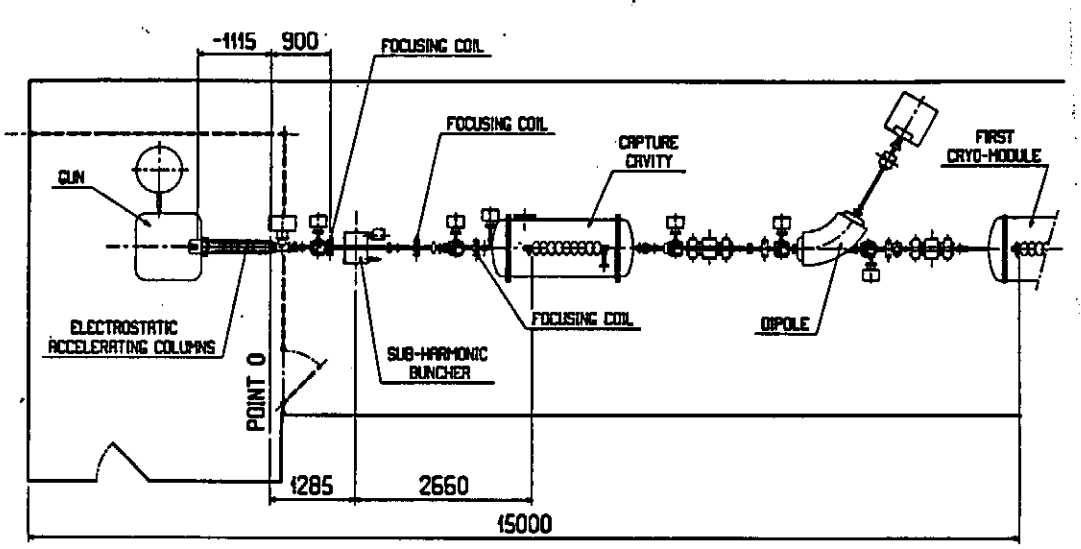

Figure 6: The layout of TTF Injector #1. Distances are in mm.

is important, though, as a beam with this energy can be captured and accelerated without using reduced or graded-β sections.

For high charge injectors, it is necessary to immerse the beam (from the gun on) in a continuous solenoidal field to counteract the beam expansion due to the huge space charge forces. As this is not possible to do with the SC capture cavity, it is proposed to pre-accelerate and bunch the beam before reaching the SC cavity. To do this, one can use a 4-cell, $\beta = 1$, normal conducting (NC) buncher. Assuming a shunt impedance of 50 MΩ/m and a total length of ~50 cm, 250 kW of power is required to obtain an accelerating field of 5 MV/m. This is the same value as is required to power the SC capture cavity, so an identical klystron and modulator (which has already been studied) could be used. The structure will have to dissipate ~5 kW/m of average power for a 1% duty cycle, a number that can be reasonably obtained.

After the NC buncher, it is planned to leave the capture cavity in the same physical location as for injector #1 and use it to boost the beam energy before reaching the MB. The distance between the NC and SC cavities should be as short as possible, and the length should be surrounded by a solenoidal field. Covering the entire length is impracticle, though, and is discussed further in section 4.5.

The MB itself will require about 1.2 m of space between the SC capture cavity and the main linac. Whether or not there is sufficient space for the MB and all of the beam analysis equipment is still an open question.

A high charge injector based on the above considerations has been found to provide reasonable results. The part of the beamline including the NC buncher, the SC cavities, and the MB are roughly the same for all of the models studied. The beamline including the subharmonic bunchers varies depending on the gun voltage and initial bunch length.

4.2 Emittance Goals

It is important to have an estimate of the maximum allowable emittance for injector #2 as a goal for the simulations. If one assumes that the beam can have a maximum radius of 1 cm, and considering that the injected beam be transported through the linac unaccelerated, the admittance of the TTF linac can be estimated in the following manner. The average beta function for the periodic line is $\beta_{avg} = \frac{L}{\sin \mu}$ where L= 12 m is the distance between quadrupoles, and $\mu = 90°$ is the phase advance. Then, the admittance is given by $\epsilon = \frac{r^2}{\beta} = 8\ \beta\ \gamma\ \pi$ mm-mrad. For example, a beam energy of 18 MeV implies a maximum emittance of 290 π mm-mrad.

4.3 Thermionic Gun Model

A model for injector #2 using a thermionic gun is based on a design for the NLC injector described by R. Miller [5]. The gun is assumed to operate at 262 kV and emit $5 \times 10^{10}\ e^-$ in a rectangular pulse 350 ps wide. A gun with similar properties, 170 kV and $2 \times 10^{10}\ e^-$ in 350 ps FWHM (700 ps FW) has been reported [13]. Similarly to the NLC model, the gun is followed by two 650 MHz subharmonic bunchers separated by $\sim$ 50 cm, with another 25 cm drift before entering the NC buncher. There is solenoidal focusing to the end of the NC buncher, then a drift space and a final, discrete solenoid at the entrance to the cryostat (see figure 7 for a magnetic field profile). The beam is then accelerated to $\sim$18 MeV and focused by a quadrupole triplet into a magnetic buncher with R_{56} = 0.168 cm/%, L_m = 15 cm, $\alpha = 27.5°$, L_1 = 21.75 cm, and L_2 = 20 cm. A schematic representation of the injector in shown in figure 8 (a) and the PARMELA input deck is shown in Appendix C. Figure 11 (see Appendix F for all PARMELA output) shows the x and y beam envelopes and the phase compression envelope from a PARMELA run. Figure 12 shows the emittance growth versus distance along the beamline. Figures 13 through 17 shows the phase space plots at the entrance to SHB1, the entrance to SHB2, the exit of the NC buncher, the entrance of the MB, and the exit of the MB.

The bunch length is compressed by a factor of $\sim$30 throughout the injector to reach the desired length. The first SHB compresses the bunch by a factor of 2, and the second by a factor of 1.5. The NC buncher compresses by 3.7, and the MB by a final factor of 3.4. Some debunching occurs in the drift spaces. The emittance grows from 15 π mm-mrad to 180 π mm-mrad at the entrance to the MB. The horizontal emittance grows further to 260 π mm-mrad, which is still within the emittance limit at this energy. All

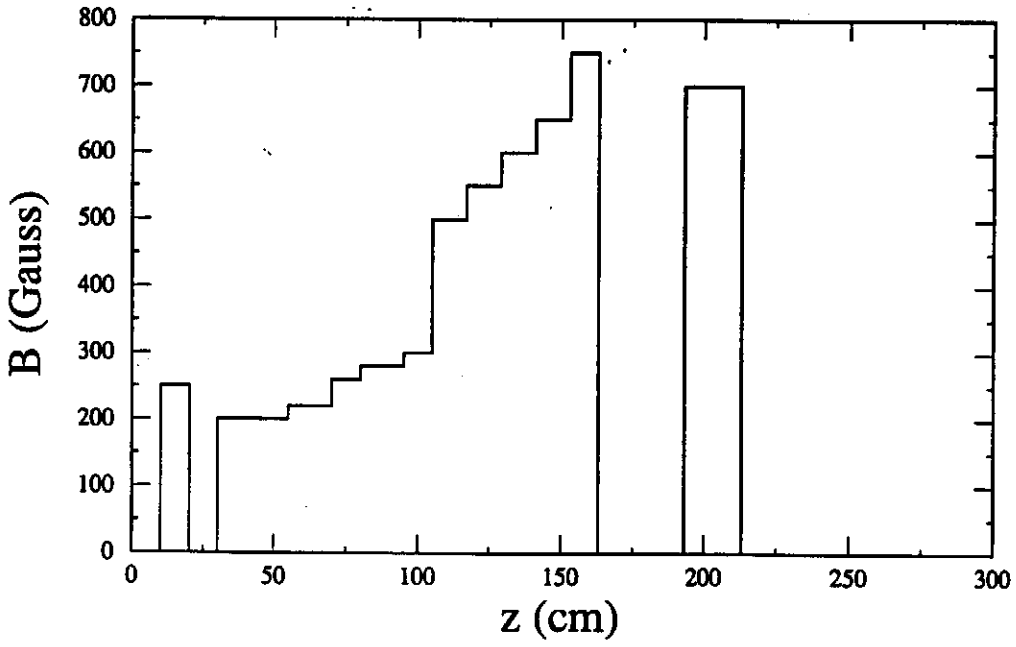

Figure 7: The magnetic field profile for the thermionic gun model.

of the parameters were optimized to keep the emittance growth as small as possible while obtaining a good phase compression. It is also important to note that the components of this model will easily fit into the space occupied by injector #1.

There are a number of variations of this model which are also possible. For instance, a gun with a longer pulse length (which are more readily available) will require lower frequency subharmonic bunchers and longer drift spaces. It is typically possible to reach the required bunch length, but final emittance tends to be larger. Increasing the number of cells in the NC buncher increases the energy at the entrance to the MB which reduces emittance growth, but this will depend on the available RF power. Also, additional solenoidal focusing between the NC buncher and the SC cavity reduces emittance growth (see section 4.5).

An high charge injector based on this model using a thermionic gun provides a beam meeting the requirements for injection into the main TTF linac. However, as the design depends very strongly on the gun properties, a final design can not be completed without a knowledge of the actual gun to be used.

4.4 Photocathode Gun Model

Another model starts off by using a high-voltage DC photocathode gun as an electron source. This is not exactly an off-the-shelf item, but it has

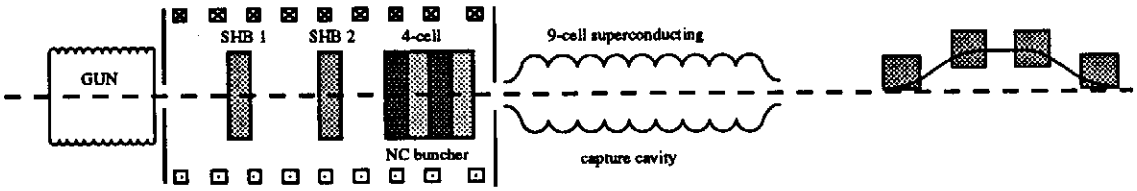

(a) Thermionic injector model

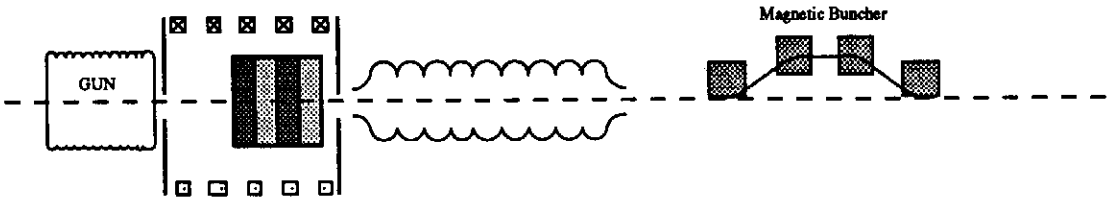

(b) Photocathode injector model

Figure 8: A schematic of the thermionic and photocathode gun injector models.

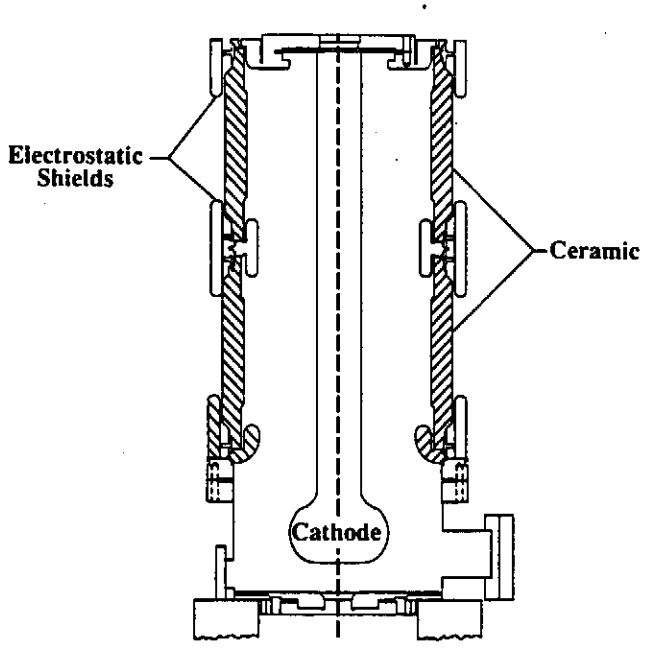

Figure 9: A schematic of the CEBAF photocathode gun (from [14]).

properties which are interesting enough to warrant an investigation. Such a gun is now under construction at CEBAF [14] (see figure 9) for use as an injector for their FEL project, and is designed to produce 0.12 nC, 100 ps bunches at 500 keV using a GaAs photocathode. Simulations show [15] that it is capable of producing the 8 nC bunches needed for injector #2.

The ability to generate 100 ps (60° of RF phase) bunches obviates the need for subharmonic bunching, and allows direct injection into the NC capture section. This feature makes the injector much more compact and reduces the number of components in the beamline. Some disadvantages are the need for semiconductor photocathode processing techniques, as well as an expensive laser system. The skills and equipment needed for operating such a gun would not be lost, though, as they would be applicable to the use of an RF gun in the future, either for TTF or for TESLA. In addition, since the gun needs only a 500 kV DC power supply (commercially available) for operation, a complicated and space consuming modulator is not required.

Another important consideration is the issue of cathode lifetime. Thermionic guns have an essentially infinite lifetime, but the lifetime of photocathode guns depend strongly on the surface quality of the cathode. In particular, for semiconductor cathodes (which are needed in this application for their high quantum efficiencies as compared to metal cathodes), the vacuum requirements are very strict. A DC photocathode gun operates

in the 10^{-11} Torr range with typical lifetimes of hundreds of hours, while an RF gun will have vacuum levels over 10 times higher due to the high power dissipation in the RF cavities, and thus a shorter lifetime. So a DC photocathode gun can be expected to have longer lifetimes than for an RF gun (using the same type of semiconductor cathode), although the beam properties may not be as good.

A schematic representation of the injector is shown in figure 8 (b), and appendix D shows the PARMELA deck used for this simulation. Figure 18 shows the x and y beam envelopes and the phase compression envelope, and figure 19 shows the emittance growth versus distance along the beamline. Figures 20 through 24 shows the phase space plots at the entrance to the NC section, the exit of the NC section, the exit of the 9-cell cavity, the entrance of the MB, and the exit of the MB.

In this simulation, the pulse debunches by ~30% in the 50 cm space from the exit of the gun to the entrance of the NC buncher. This implies that this distance should be a small as possible to reduce the debunching, as well as to reduce emittance growth due to space charge. The NC section is phased to accelerate the beam to 2.3 MeV and bunch it to $\sigma_\phi = 8.6°$ all while minimizing the emittance growth. Further bunching occurs in the drift to the SC cavities, where the beam is accelerated to 15 MeV. At the entrance to the MB, $\sigma_\phi = 8.0°$, and $R_{56} = -.055$. A pair of slits between the two central magnets of the MB, located at ± 0.9 cm from the central trajectory, scrape off the high and low energy tails of the bunch. This results in a bunch length of $\sigma = 1.3°$ at the end of the MB and a reduction in particle number from 6×10^{10} e^- to 4.8×10^{10} e^-. The emittance grows from 40 π mm-mrad to 180 π mm-mrad, and the final energy spread is $\sigma_E = 975$ keV.

The initial emittance of 40 π was a somewhat arbitrary choice. A simulation of the CEBAF gun from the cathode to the gun exit was performed [15] using the point-to-point method with a PARMELA version modified to include the electrostatic fields. The model included only the gun with no external focusing, and gave a resulting emittance of 133 π mm-mrad (90%, unnormalized) and a beam radius (diverging) of 2.6 cm. Using these results, another simulation of the photocathode injector was performed (see Appendix E). In this case, it was possible to reach a final bunch length of 2.2° without using a MB. The resulting emittance is high, though (300 π) and the energy is low (13 MeV). Figure 25 shows the envelope plots, and figure 26 shows the phase space plots after passing through the quadrupole triplet. Table 2 shows results for several different phases of the NC and SC cavities for this model: it is possible to have a higher energy beam and lower emittance, but a MB is required for these cases.

The models utilizing a 500 keV photocathode gun provide a beam meeting the requirements for injector #2. The system will take up less space than the thermionic injector and without subharmonic bunchers the RF system will be simpler. A photocathode gun, however, is more complicated to operate and needs a sophisticated laser system. Further studies will include

ϕ_{NC} (o)	ϕ_{SC} (o)	E (MeV)	σ_E (keV)	$\epsilon_{n,4-rms}$ (π mm-mrad)	e^-_{in} / e^-_{out} ($\times 10^{10}$)	R_{56} (cm/%)	ϕ_{final} (°)
180	110	13.0	186	300	5/5	-	2.2
185	130	15.5	704	250	6/6	0.05	1.5
180	140	17.5	200	240	6/4.8	0.10	2.2

Table 2: Results for the photocathode model using a realistic initial emittance. ϕ_{NC} and ϕ_{SC} are the phases of the first cell of the normal conducting and the superconducting cavities, respectively.

modeling the injector from the cathode through the MB instead of using a PARMELA input card to emulate the initial emittance and beam size at the gun exit.

4.5 Is a Superconducting Solenoid Necessary?

Simulations have shown that it is beneficial to have solenoidal focusing all along the distance between the exit of the RF buncher and the first iris of the 9-cell SC cavity. It is obvious that mechanical constraints of the crytostat will prohibit this, however. It is possible to have solenoids as close as 50 cm from the first iris and still be outside of the cryostat, and it is possible to have one SC solenoid 25 cm from the iris [16].

As a SC solenoid will cause extra difficulty and expense in the construction of the cryostat, a comparison between runs with and without a SC solenoid were performed. Figure 10 shows the results of the simulation using the thermionic gun model. In the beam envelope, one can clearly see the difference between the two cases, and the emittance is lower by 25 π when the SC solenoid in on. Whether the benefits gained by this are worth the expense or not is not clear. If possible, a SC solenoid should be included, as it will be much harder to add it on later if it is found to be necessary during operation.

5 Conclusion and Future Work

From the simulations performed for this report, one can conclude that an injector can be built that will fulfill the requirements for a high charge injector for the TESLA test facility. The emittance becomes quite large, but it is generally in the range of the emittance limitation set here. Such an injector would consist of an electron gun (either thermionic or photocathode), two subharmonic bunchers (not necessary for the photocathode gun), a 4-cell, normal conducting buncher, a 9-cell superconducting structure, and a magnetic buncher.

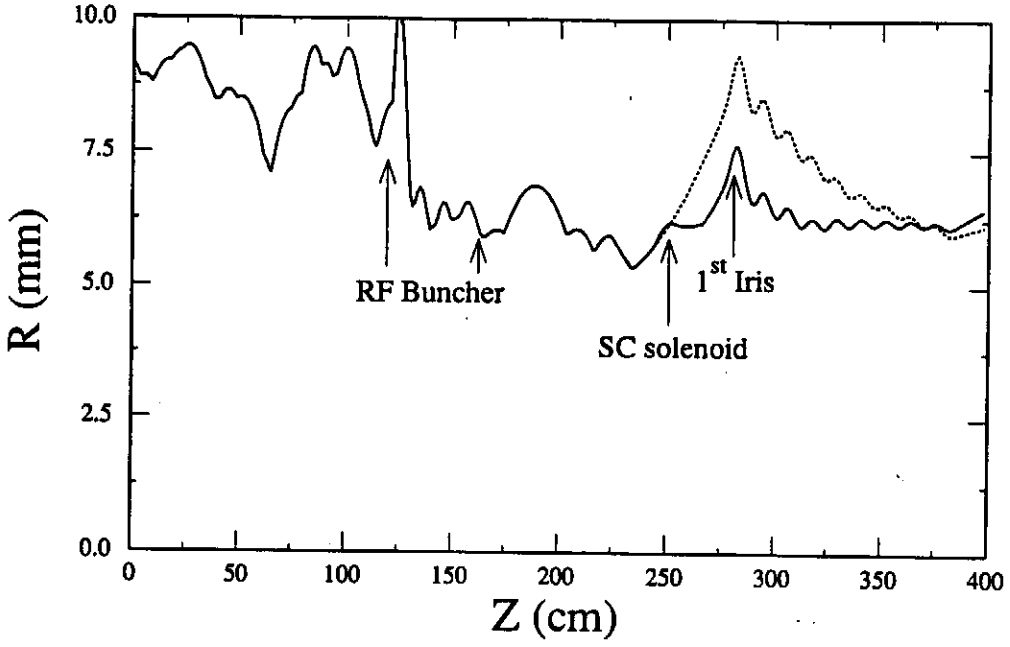

Figure 10: The beam envelopes with (solid line) and without (dotted line) a superconducting solenoid.

The use of the PARMELA space charge routines has been studied with regards to the applications discussed here. It has been found that one must be very careful in setting the space charge calculation parameters in order to find consistent results as the parameters are varied. Practical experience shows that the results from PARMELA can vary by a factor of 2 when compared with measurements.

The exact details of the models depend very strongly on the actual properties of the electron gun to be used. For future simulations, the model should include the measured parameters of an existing gun, as well as more realistic characterizations of the rest of the elements of the injector. Effects such as wakefields, beam loading, and instabilities have not been included.

References

[1] G. Mavrogenes *et al.*, IEEE Trans. Nucl. Sci. **NS-30**, 2989 (1983).

[2] A. Yeremian *et al.*, "SLC Injector Simulation and Tuning for High Charge Transport", *Proc. 1992 Linear Accelerator Conf.*, 353 (1992)

[3] A. Yeremian *et al.*, "Boeing 120 MeV RF Linac Injector Design and Accelerator Performance Comparison with PARMELA", *Proc. of the 1989 IEEE Particle Accelerator Conference* 657 (1989).

[4] S. Takeda *et al.*, "High Current Single Bunch Electron Linear Accelerator", IEEE Trans. Nucl. Sci. **NS-32** 3219 (1985).

[5] R. Miller, presented at the TESLA collaboration meeting, Fermilab, 1993.

[6] K. Crandall and L. Young, "PARMELA: Phase and Radial Motion in Electron Linear Accelerators", private communication

[7] B. Carlsten, "High Peak Current, Low Emittance Electron Pulses at Medium Energy", *Proc. 1990 Linear Accelerator Conf.* 641 (1990).

[8] T. Raubenheimer, Workshop on Fourth Generation Light Sources, SSRL, 263 (1992).

[9] H. Liu, "Analysis of Space Charge Calculation in PARMELA and its Application to the CEBAF FEL Injector Design", **CEBAF PR 93-23.**

[10] K. MacDonald, IEEE Trans. Elec. Dev., **35** 2052 (1988).

[11] M. Jablonka and E. Klein, TESLA report **93-05**

[12] T. Garvey, private communication

[13] H. Matsumoto *et al.*, "High-Gradient S–Band Test Linac for Japan Linear Collider", *Proc. 1992 Linear Accelerator Conf.*, 296 (1992)

[14] C. K. Sinclair, "A 500 kV Photoemission Electron Gun for the CEBAF FEL", Nucl. Instr. and Meth. **A318**, 410 (1992)

[15] D. Engwall, private communication

[16] T. Junquera, private communication

A Appendix - Input Deck for A Magnetic Buncher

```
run /n0= 1 / 1 /freq=  1300. MHz/zo= -0 cm/eo= 7. Mev/ 4
bend 15 20 1 6.5 30 0 30 0 0 0 0
drift 7 20 1
bend 15 20 1 6.5 -30 -30 0 0 0 0 0
bend 15 20 1 6.5 -30 0 -30 0 0 0 0
drift 7 20 1
bend 15 20 1 6.5 30 30 0 0 0 0 0
output 5
input 8 499 0 1 14 0 1 14 11.87 166.6 .01 0 0 0 0 10 .6
scheff -5e10 1.8 12 40 10 0 0 1 1.5 0 0
start 0. 5 50500 1 1
end
```

B Appendix - Subroutine for field definition of 9-cell cavity

```
      SUBROUTINE CEL9FLD(R,ZC,EZ,ER,BT)
      COMPLEX B(30),CST1,CST2,V1,V2,V3
      DATA (B(I),I=1,30)/
     *  (  0.843810E-01 ,  0.000000E+00),
     *  (  0.697942E-01 ,  0.000000E+00),
     *  (  0.287447E-01 ,  0.000000E+00),
     *  ( -0.328701E-01 ,  0.000000E+00),
     *  ( -0.115581E+00 ,  0.000000E+00),
     *  ( -0.300888E+00 ,  0.000000E+00),
     *  (  0.333334E+00 ,  0.000000E+00),
     *  (  0.236678E-01 ,  0.000000E+00),
     *  ( -0.153335E-01 ,  0.000000E+00),
     *  ( -0.186133E-01 ,  0.000000E+00),
     *  ( -0.115547E-01 ,  0.000000E+00,
     *  ( -0.373767E-02 ,  0.000000E+00),
     *  (  0.748970E-03 ,  0.000000E+00),
     *  (  0.116632E-02 ,  0.000000E+00),
     *  ( -0.135633E-02 ,  0.000000E+00),
     *  ( -0.519317E-02 ,  0.000000E+00),
     *  ( -0.960553E-02 ,  0.000000E+00),
     *  (  0.243867E-01 ,  0.000000E+00),
     *  ( -0.375515E-02 ,  0.000000E+00),
     *  ( -0.348522E-02 ,  0.000000E+00),
```

```
*  ( -0.200690E-02 ,  0.000000E+00),
*  ( -0.625671E-03 ,  0.000000E+00),
*  (  0.229279E-03 ,  0.000000E+00),
*  (  0.448254E-03 ,  0.000000E+00),
*  (  0.221036E-03 ,  0.000000E+00),
*  ( -0.169151E-03 ,  0.000000E+00),
*  ( -0.437015E-03 ,  0.000000E+00),
*  ( -0.346162E-03 ,  0.000000E+00),
*  (  0.232013E-02 ,  0.000000E+00),
*  ( -0.104627E-02 ,  0.000000E+00)/

   ZI=ZC*10.0
   CST1=-2*3.14159265358979/1300.*(0.,1.)
   CST2=ZI*CST1
   IF (ZI.LT.0. .OR. ZI.GT.1300.) THEN
      ER=0.0
      EZ=0.0
      BT=0.0
      RETURN
   END IF
   OU=B(1)
   OUD=0.0
   DO  J=2,30
      V1=(J-1)*CST1
      V2=(J-1)*CST2
      V3=B(J)*CEXP(V2)
      OUD=OUD+20.*REAL(V3*V1)
      OU=OU+2.*REAL(V3)
   END DO
   EZ=(OU/100.)
   ER=(-0.5*R*OUD/100.)
   BT=(0.5*EZ)
   END
```

C Appendix - Input Deck for Thermionic Gun Model

```
run /n0= 1 / 1 /freq= 1300. MHz/zo= 0. cm/eo=.2620 Mev/type= 2
(type 2 indicates a Los Alamos side coupled structure)
drift 10 2 1
solenoid 10 2 1 250
drift 10 2 1
buncher     0.     5.  1   /dV(MeV) 0.100 /fsh 650.  /phi  50
```

```
solenoid    25.    5.  1  /bmax 200.
solenoid    25.    5.  1  /bmax 220.
buncher     0.     5.  1   /dV(MeV) 0.100 /fsh 650.  /phi  245
solenoid    10.    5.  1  /bmax 260.
solenoid    15.    5.  1  /bmax 280.
solenoid    10.    5.  1  /bmax 300.
cell 11.53 5. 1 /phi= 30  /e= 7 /nc= 1 /dt= 5. /fr 1300. 0 0 500
cell 11.53 5. 1 /phi= 210 /e= 7 /nc= 2 /dt= 5. /fr 1300. 0 0 550
cell 11.53 5. 1 /phi= 30  /e= 7 /nc= 3 /dt= 5. /fr 1300. 0 0 600
cell 11.53 5. 1 /phi= 210 /e= 7 /nc= 4 /dt= 5. /fr 1300. 0 0 650
solenoid    10.    5.  1  /bmax  750.
drift 30 5 1
solenoid 20 5 1 700
drift 30 5 1
cel9t /l=130cm /ap= 2 1 /ph= 180 /e= 30 /nc= 5 /dt= 5
drift 20 5 1
drift 20 5 1
drift 20 5 1
quad 10 2 1 150.
drift 5 2 1
quad 20 2 1 -140
drift 5 2 1
quad 10 2 1 150
drift 50 2 1
drift 50 2 1
bend 15 20 1 17.6 27.5 0 27.5 0 0 0 0
drift 21.75 20 1
bend 15 20 1 17.6 -27.5 -27.5 0 0 0 0 0
drift 10 20 1
slits 0 0 1 /xmin= -.9 /xmax= .9 -20. 20.
(a rectangular slit, blocks electrons outside of - )
( -.9 < x < .9, -20 < y < 20 )
drift 10 20 1
bend 15 20 1 17.6 -27.5 0 -27.5 0 0 0 0
drift 21.75 20 1
bend 15 20 1 17.6 27.5 27.5 0 0 0 0 0
drift 20 20 1
input 6 /np= 399 / 0.  5. 20. / 0. 5. 20. / 82. 0.
(beta has units of mm/mrad, emittance has units of  pi mm-mrad)
scheff -5e10 \r= 1.5 \z= 0. \nr= 20 \nz= 30  0 0 1 1.5 0 0
(\z=0 invokes the 'auto' routine)
output 5
start -0.  20 50500 1 1
end
```

D Appendix - Input Deck for Photocathode Gun Model–1

```
run /n0= 1 / 1 /freq=  1300. MHz/zo= -1.66 cm/eo= .500 Mev/ 5
(type 5 indicates a sinusoidal accelerating field)
drift 10 2 1
solenoid    10.    2.  1  /bmax 400.
solenoid    10.    2.  1  /bmax 400.
solenoid    10.    2.  1  /bmax 350.
solenoid    10.    2.  1  /bmax 300.
cell 11.53 2. 1 /phi= 110 /e= 10 /nc= 1 /dt= 5 /fr 1300 0 0 450
cell 11.53 2. 1 /phi= 290 /e= 10 /nc= 2 /dt= 5 /fr 1300 0 0 600
cell 11.53 2. 1 /phi= 110 /e= 10 /nc= 3 /dt= 5 /fr 1300 0 0 650
cell 11.53 2. 1 /phi= 290 /e= 10 /nc= 4 /dt= 5 /fr 1300 0 0 800
drift 30 2 1
solenoid 20 2 1 800
drift 30 2 1
cel9t /l=130cm/    2.  1  /ph= 45. /e= 30.0 /nc 9 / dwt 5.
drift 20 2 1
drift 20 2 1
drift 20 2 1
drift 20 2 1
drift 20 2 1
quad 10 2 1 100.
drift 5 2 1
quad 20 2 1 -100
drift 5 2 1
quad 10 2 1 100
drift 50 2 1
drift 50 2 1
bend 15 20 1 15. 20 0 20 0 0 0 0
drift 7 20 1
bend 15 20 1 15. -20 -20 0 0 0 0 0
slits 0 0 1 -.9 .9 -20. 20.
bend 15 20 1 15. -20 0 -20 0 0 0 0
drift 7 20 1
bend 15 20 1 15. 20 20 0 0 0 0 0
drift 20 20 1
output 5
input 6 /np= 999 / 0. 1. 40. / 0. 1. 40. / 30. 0.002
scheff  -6e10  1.  0.  20   30   0  0.  1 1.5 0 0
start /phio= -30  /dWt= 10. /nst= 16000 /nsc= 1 nout= 1 /
end
```

E Appendix - Input Deck for Photocathode Gun Model–2

```
run /n0= 1 / 1 /freq=1300. MHz/zo= -1.66 cm/eo=.500 Mev/type= 4
(type 4 indicates a Chalk River structure)
drift /l= 10 /aper= 4 /iout= 1
solenoid /l= 10 /aper= 4 1 300
drift /l= 10 /aper= 4 1
drift /l= 10 /aper= 4 1
drift /l= 10 /aper= 4 1
cell 11.53 3. 1 /phi= 180 /e= 8 /nc= 1 /dt= 5 /fr 1300. 0 0 350
cell 11.53 3. 1 /phi= 360 /e= 8 /nc= 2 /dt= 5 /fr 1300. 0 0 400
cell 11.53 3. 1 /phi= 180 /e= 8 /nc= 3 /dt= 5 /fr 1300. 0 0 650
cell 11.53 3. 1  phi= 360 /e= 8 /nc= 4 /dt= 5 /fr 1300. 0 0 700
drift 30 2 1
solenoid 20 2 1 600
drift 30 2 1
cel9t /l=130cm/   /aper=2.  1 /ph= 110. /e= 30.0 /nc 9 /dwt 5.
drift /l= 20 /aper=  2 1
drift /l= 20 /aper=  2 1
drift /l= 20 /aper= 2 1
drift /l= 20 /aper= 2 1
quad  /l= 10 /aper= 2 1 110.
drift /l= 5 /aper= 2 1
quad  /l= 20 /aper= 2 1 -110
drift /l= 5 /aper= 2 1
quad  /l= 10 /aper= 2 1 110
drift /l= 50 /aper=2 1
drift /l= 50 /aper=2 1
output 5
input 6 /np= 499 / 0. 4.4 133 / 0. 4.4 133 / 30. 0.002
(beta has units of mm/mrad, emittance has units of  pi mm-mrad)
scheff -5e10 /dr= 2.2 /dz= 0. /nr= 30 /nz= 30 0 0 1 /frm= 1.5
start /phio= -30  /dWt= 5. /nst= 16000 /nsc= 1 nout= 1 /
end
```

F Appendix - PARMELA Graphic Output

- Figure 11 - The beam and phase envelopes for the thermionic model.
- Figure 12 - The emittance growth along the beamline for the thermionic model.
- Figure 13 - The output at the entrance to SHB1 for the thermionic model.
- Figure 14 - The output at the entrance to SHB2 for the thermionic model.
- Figure 15 - The output at the entrance of the RF buncher for the thermionic model.
- Figure 16 - The output at the entrance to the magnetic buncher for the thermionic model.
- Figure 17 - The output at the end of the magnetic buncher for the thermionic model.
- Figure 18 - The beam and phase envelopes for the first photocathode model.
- Figure 19 - The emittance growth along the beamline for the first photocathode model.
- Figure 20 - The output at the entrance to the NC cavity for the first photocathode model.
- Figure 21 - The output at the exit of the NC cavity for the first photocathode model.
- Figure 22 - The output at the exit of the 9-cell SC cavity for the first photocathode model.
- Figure 23 - The output at the entrance of the magnetic buncher for the first photocathode model.
- Figure 24 - The output at the end of the magnetic buncher for the first photocathode model.
- Figure 25 - The beam and phase envelopes for the second photocathode model.
- Figure 26 - The output at the end of the simulation for the second photocathode model.

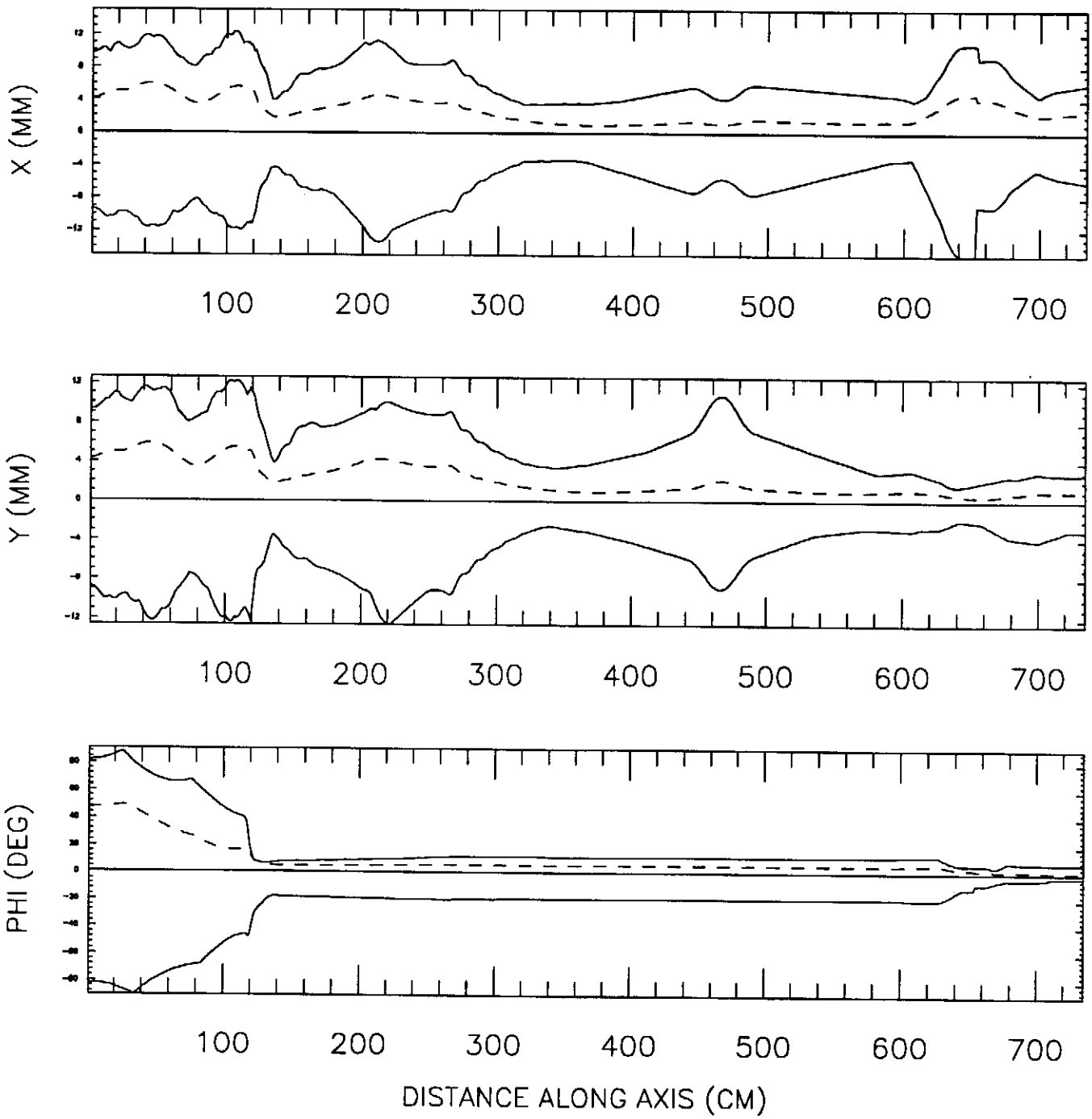

Figure 11: The beam and phase envelopes for the thermionic model.

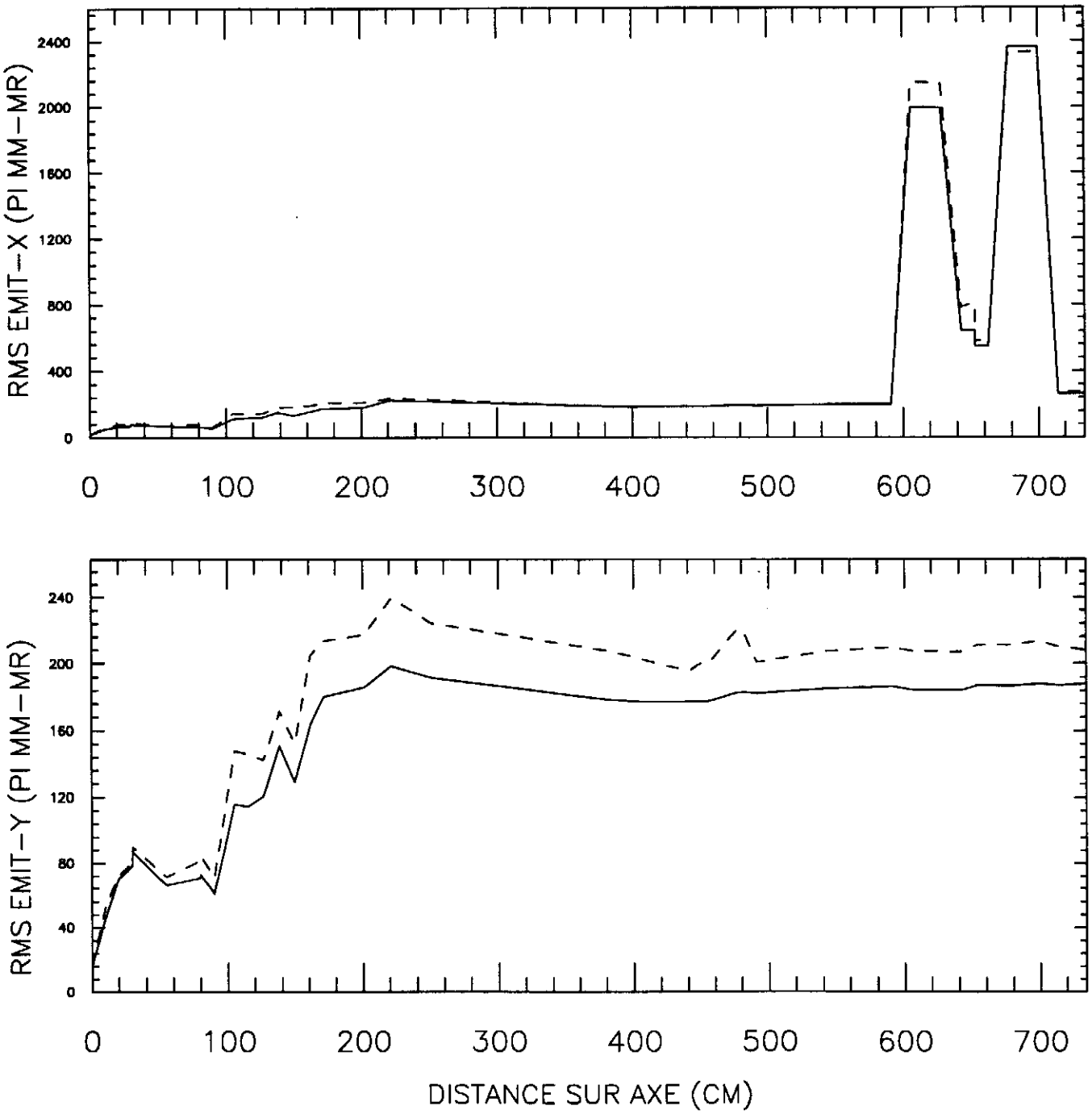

Figure 12: The emittance growth along the beamline for the thermionic model.

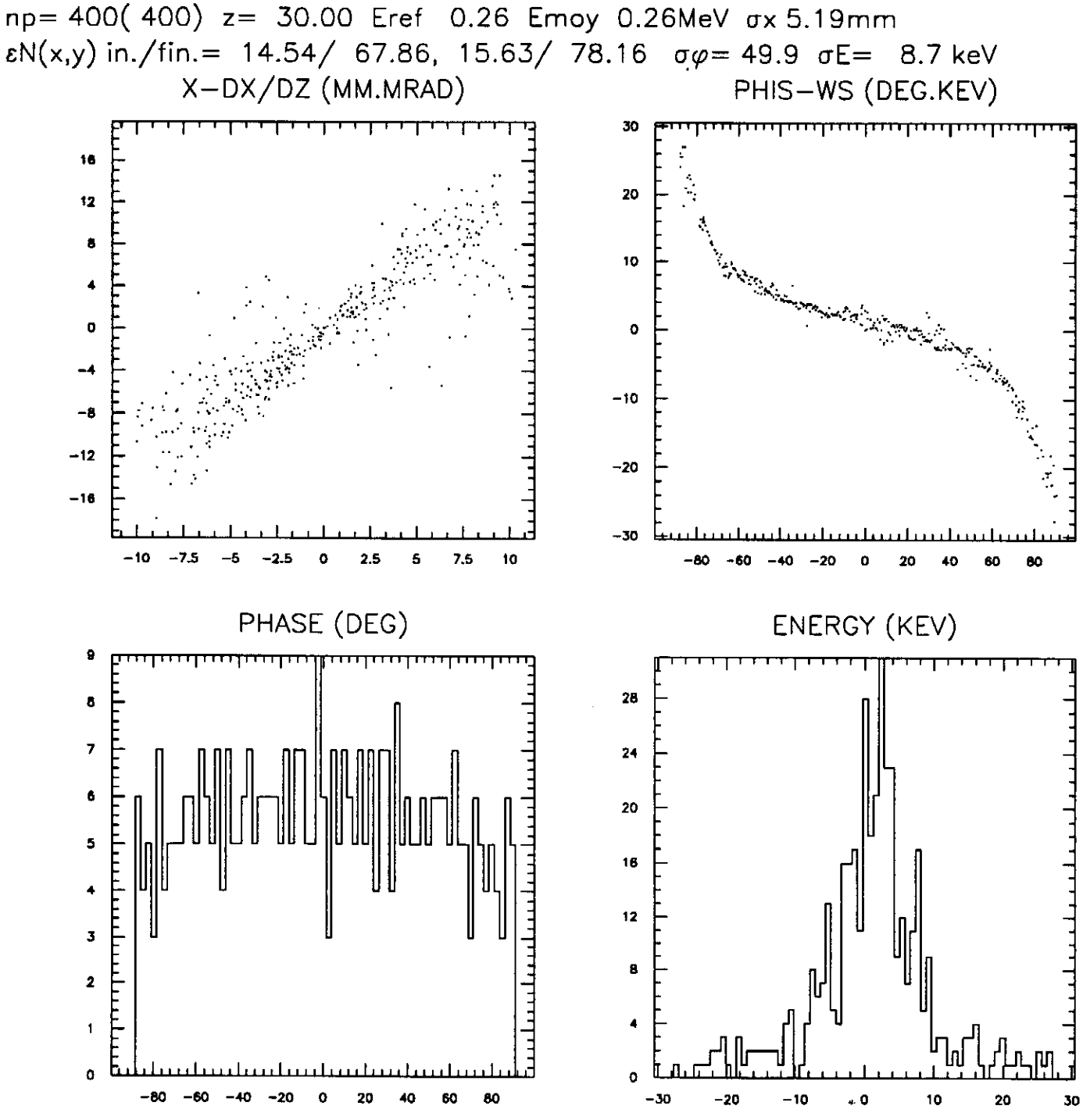

Figure 13: The output at the entrance to SHB1 for the thermionic model.

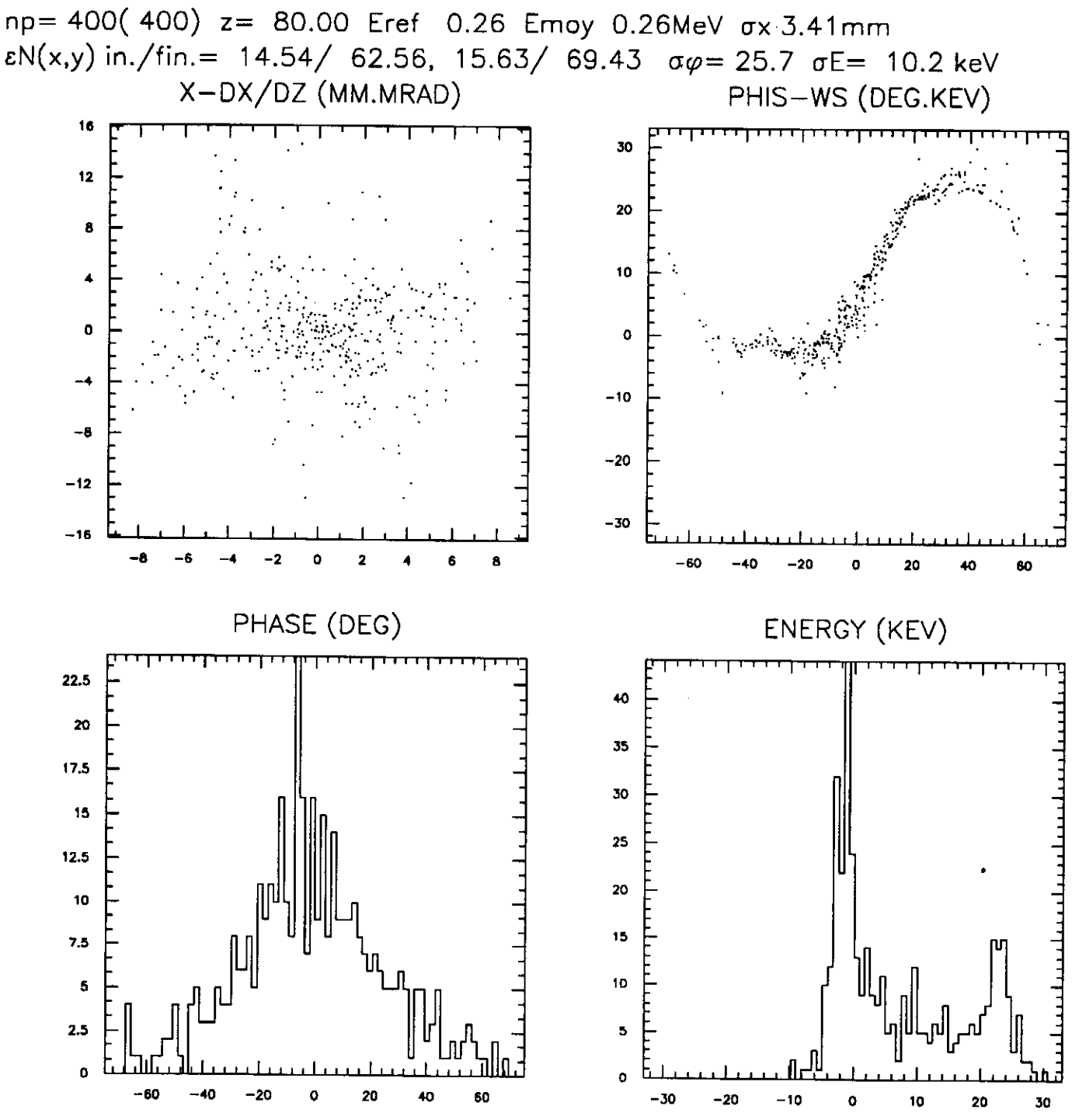

Figure 14: The output at the entrance to SHB2 for the thermionic model.

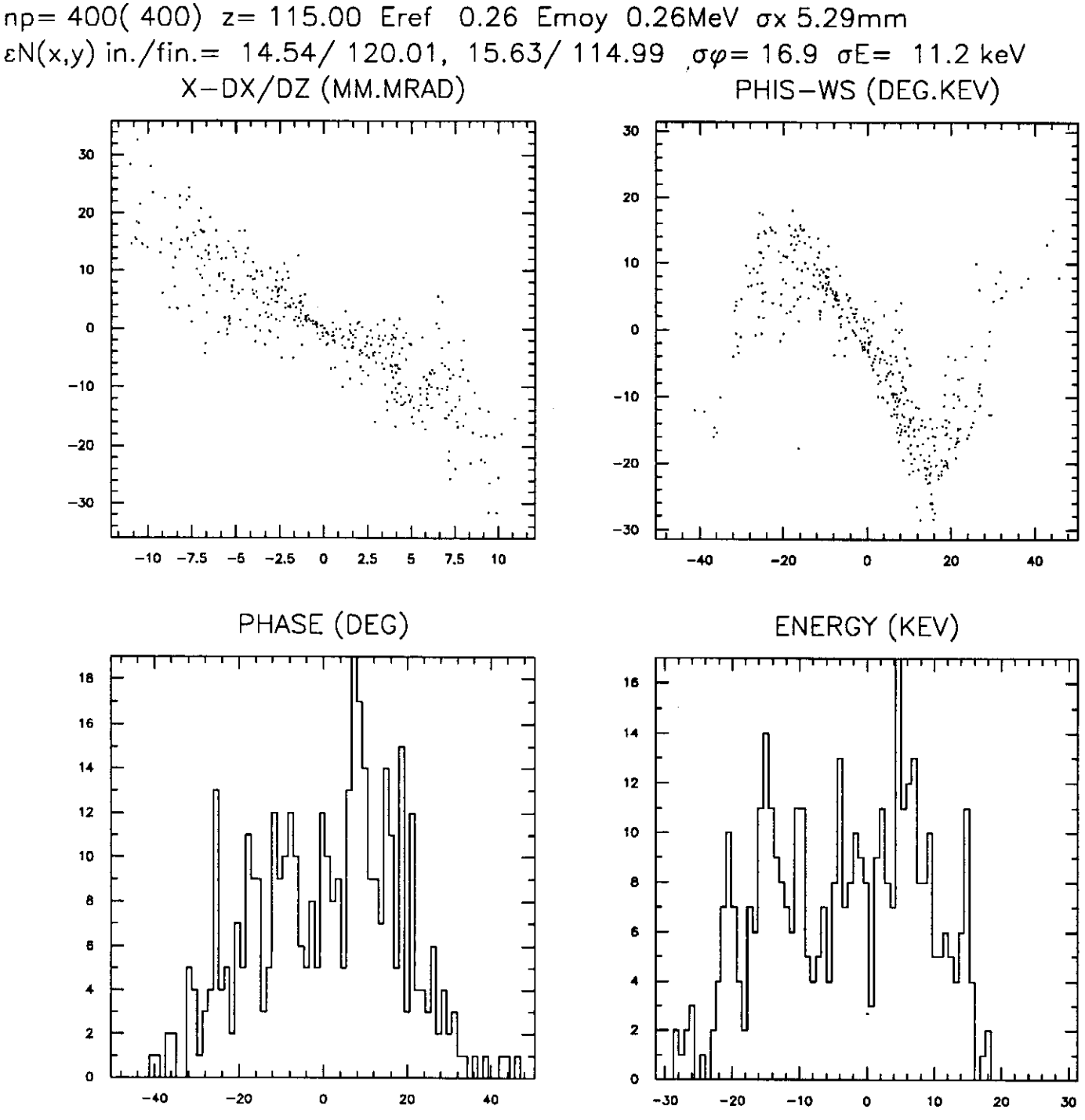

Figure 15: The output at the entrance of the RF buncher for the thermionic model.

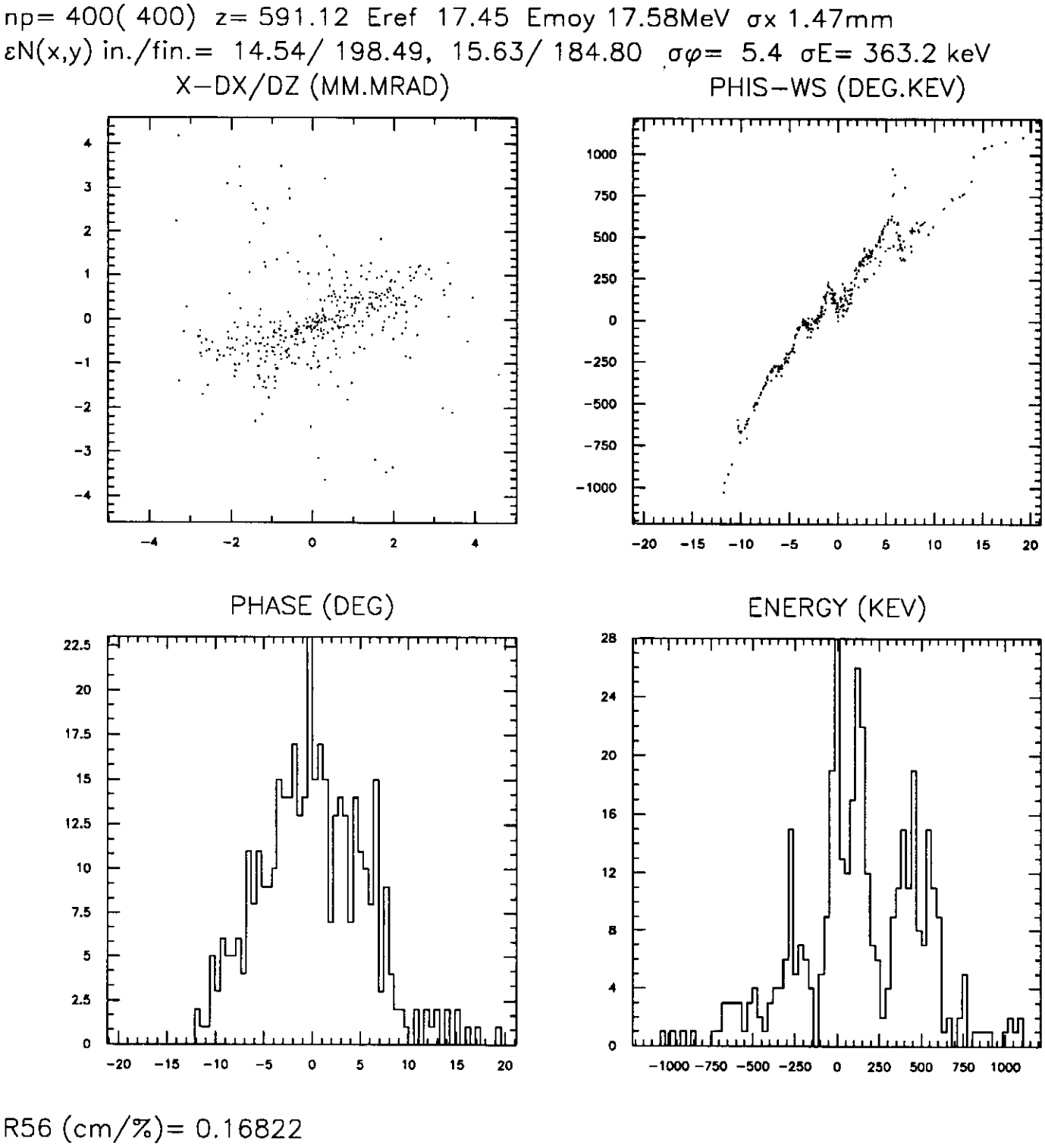

Figure 16: The output at the entrance to the magnetic buncher for the thermionic model.

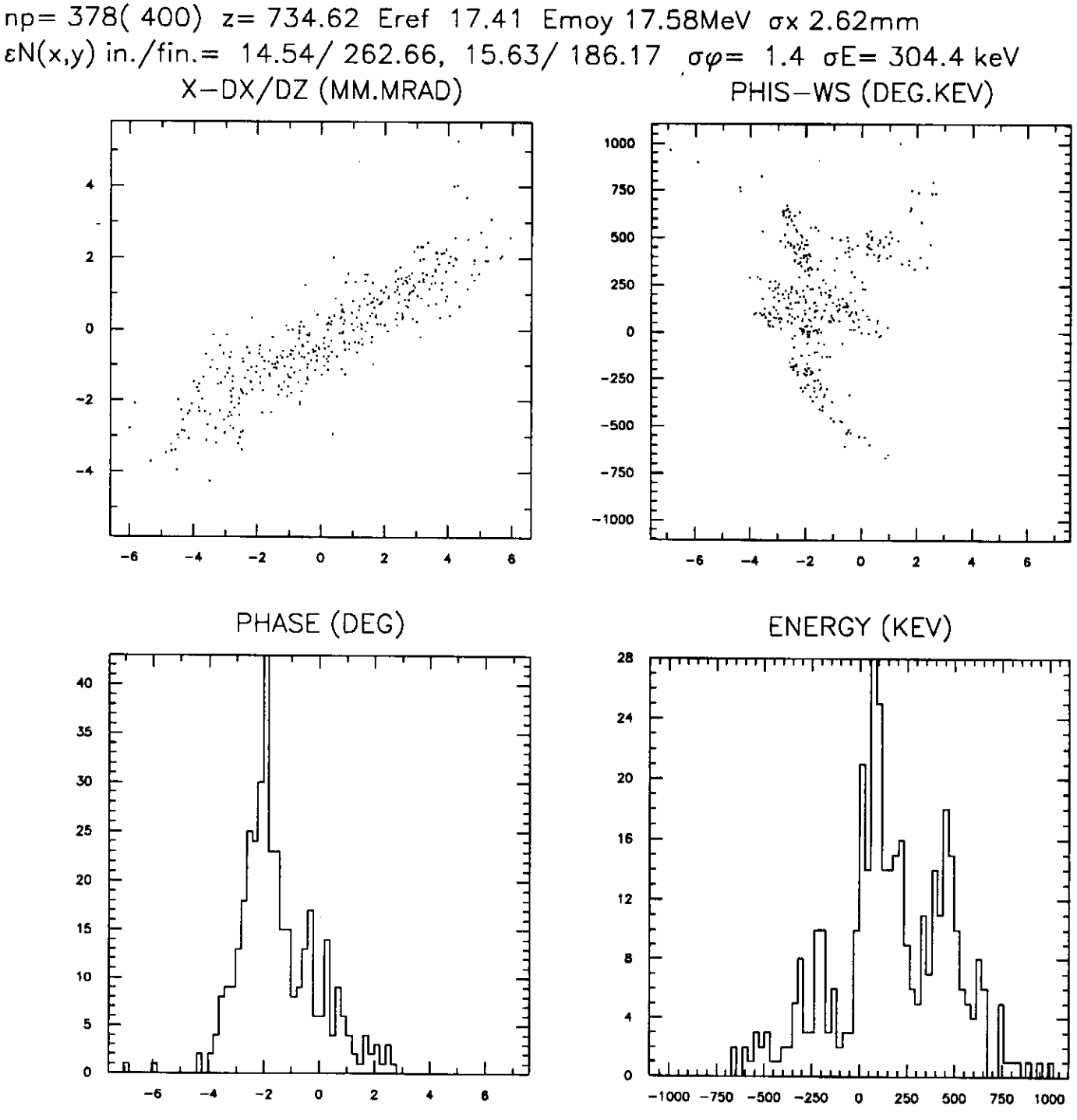

Figure 17: The output at the end of the magnetic buncher for the thermionic model.

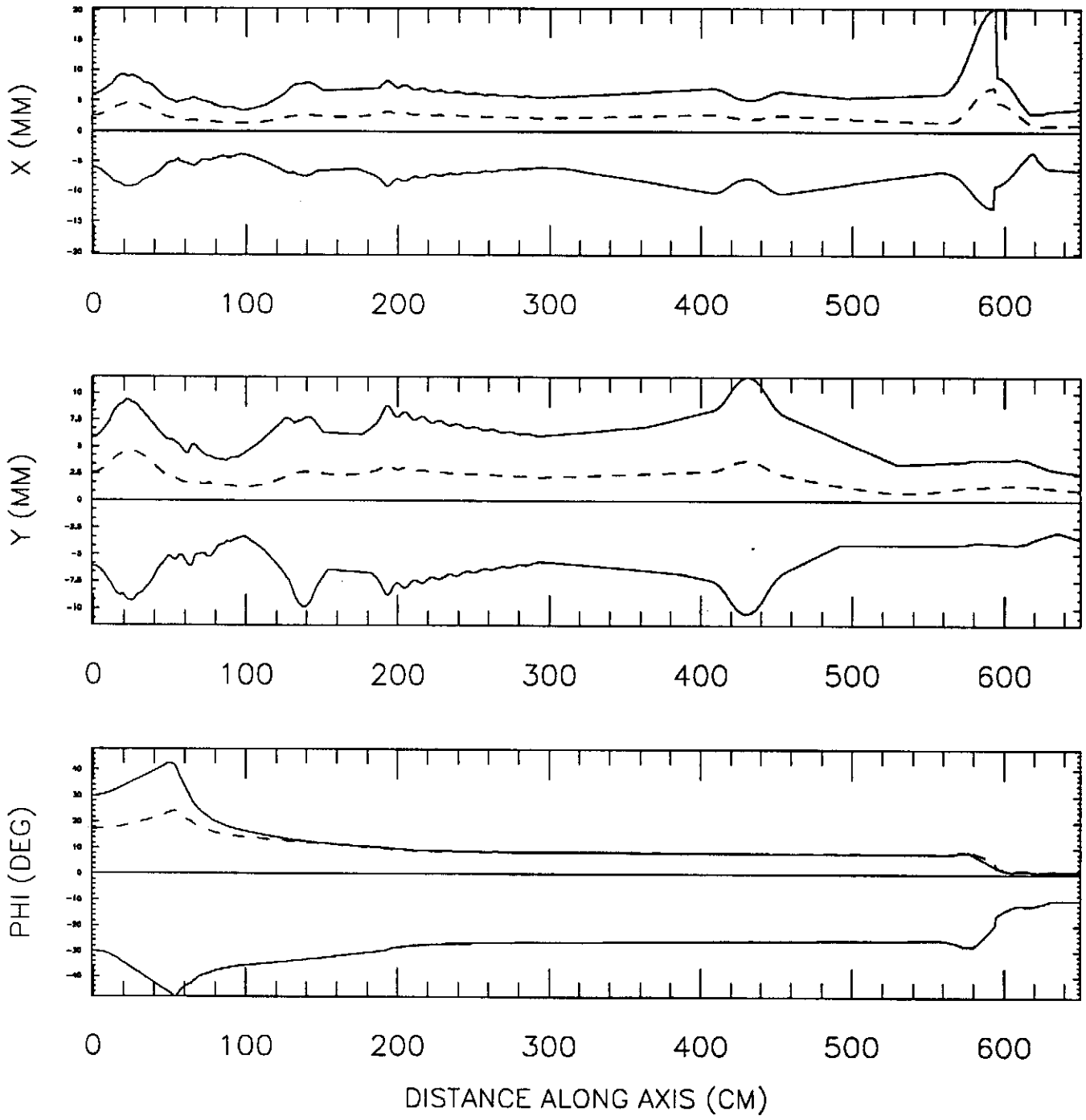

Figure 18: The beam and phase envelopes for the first photocathode model.

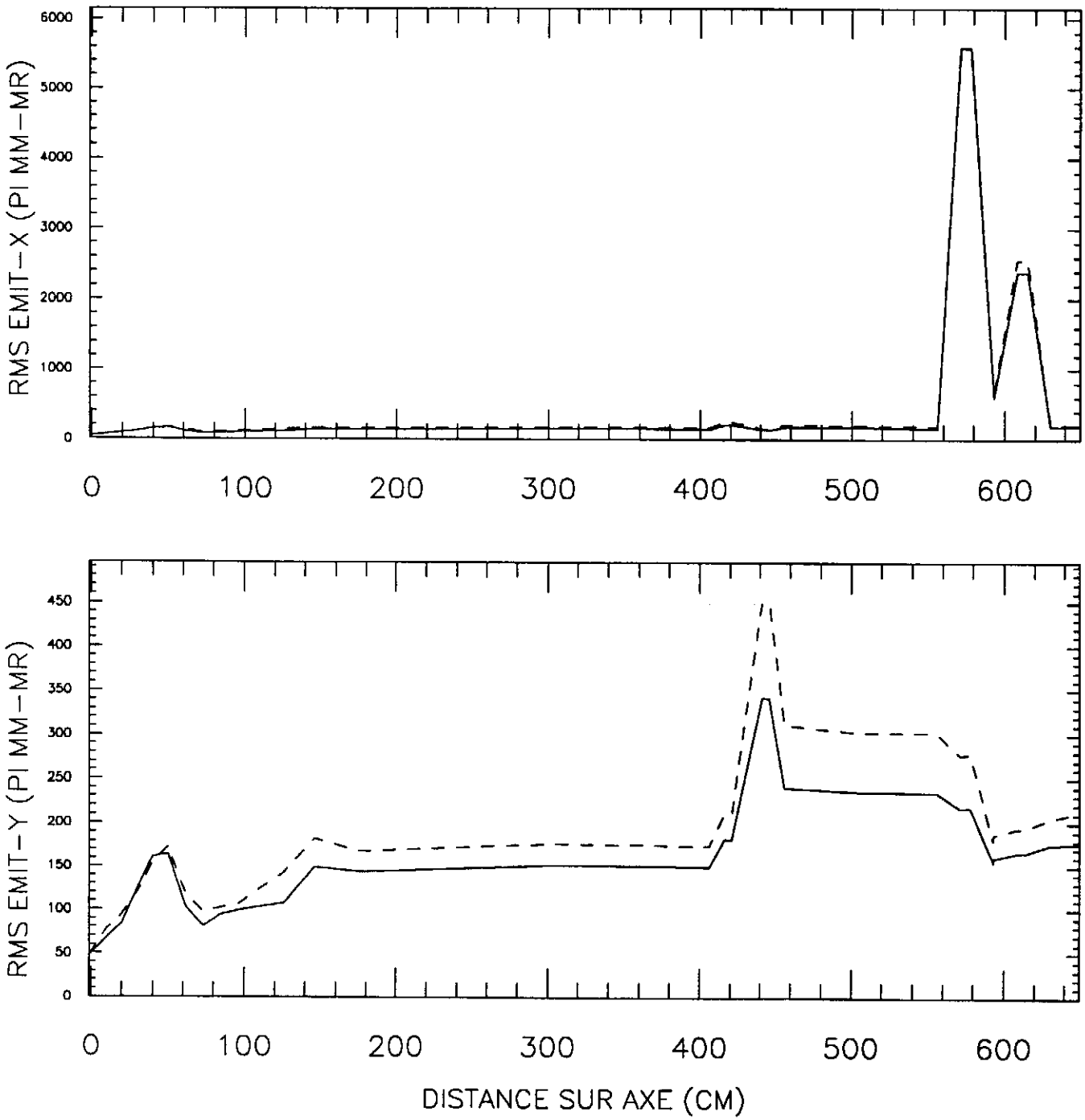

Figure 19: The emittance growth along the beamline for the first photocathode model.

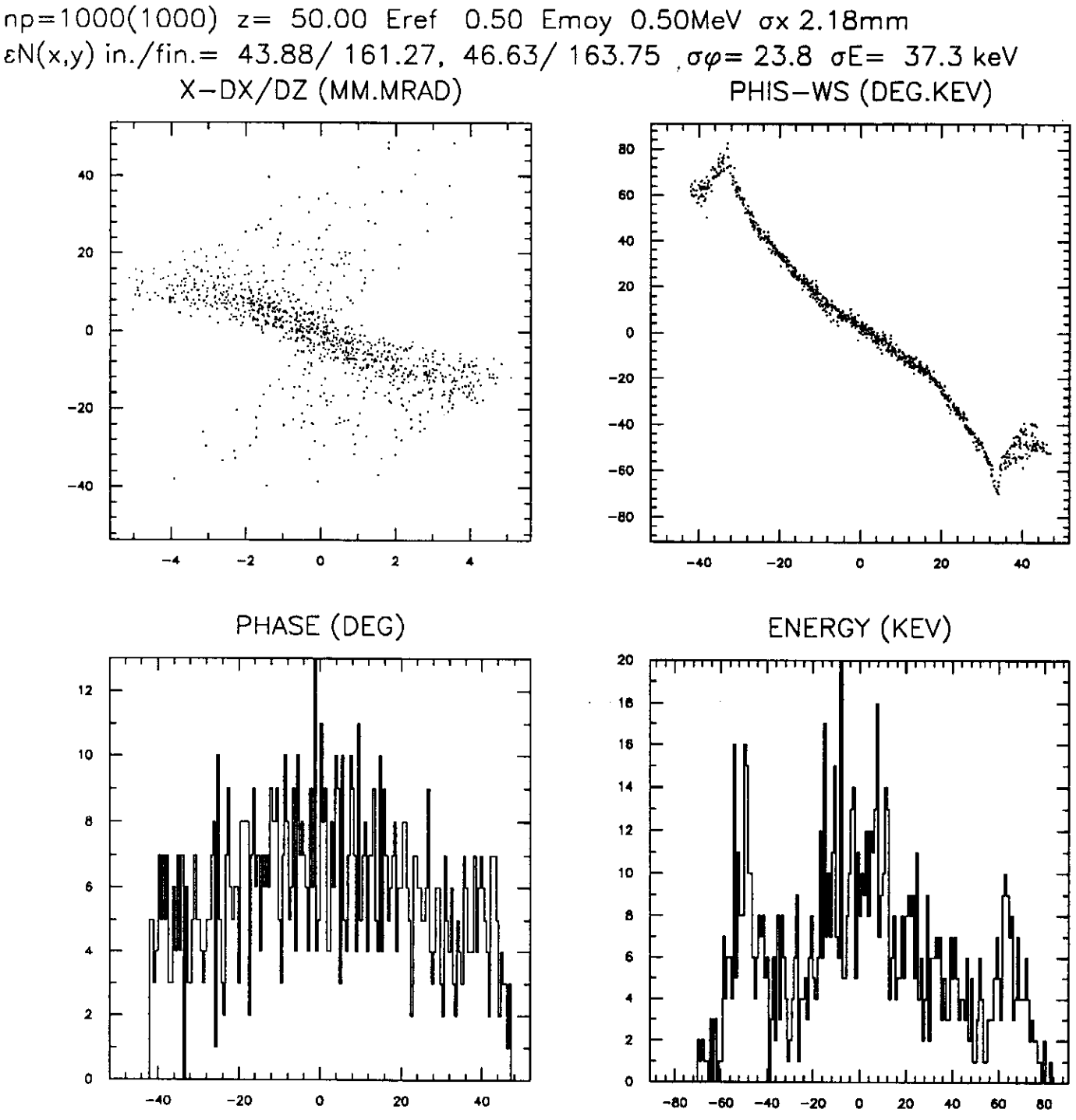

Figure 20: The output at the entrance to the NC cavity for the first photocathode model.

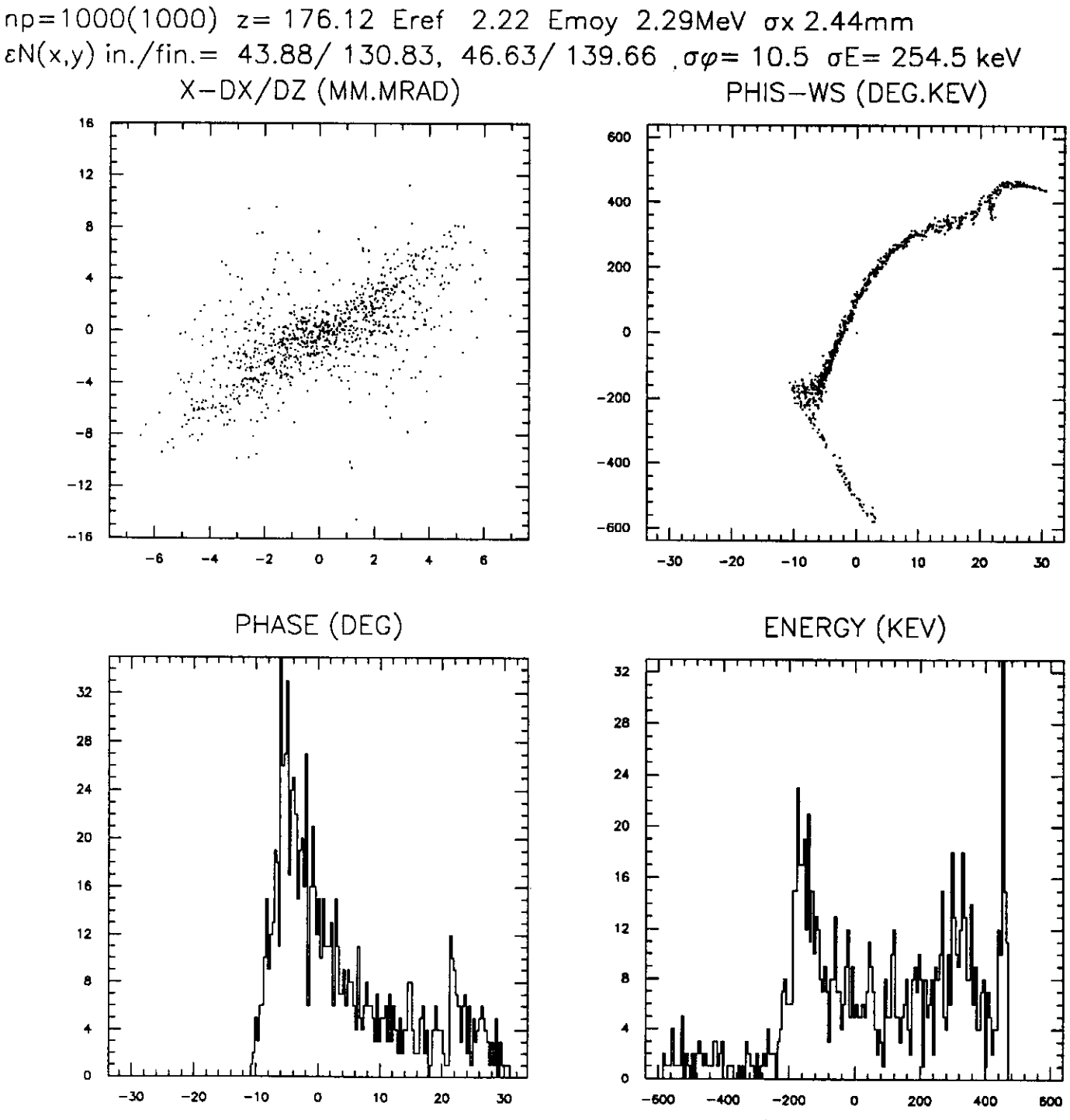

Figure 21: The output at the exit of the NC cavity for the first photocathode model.

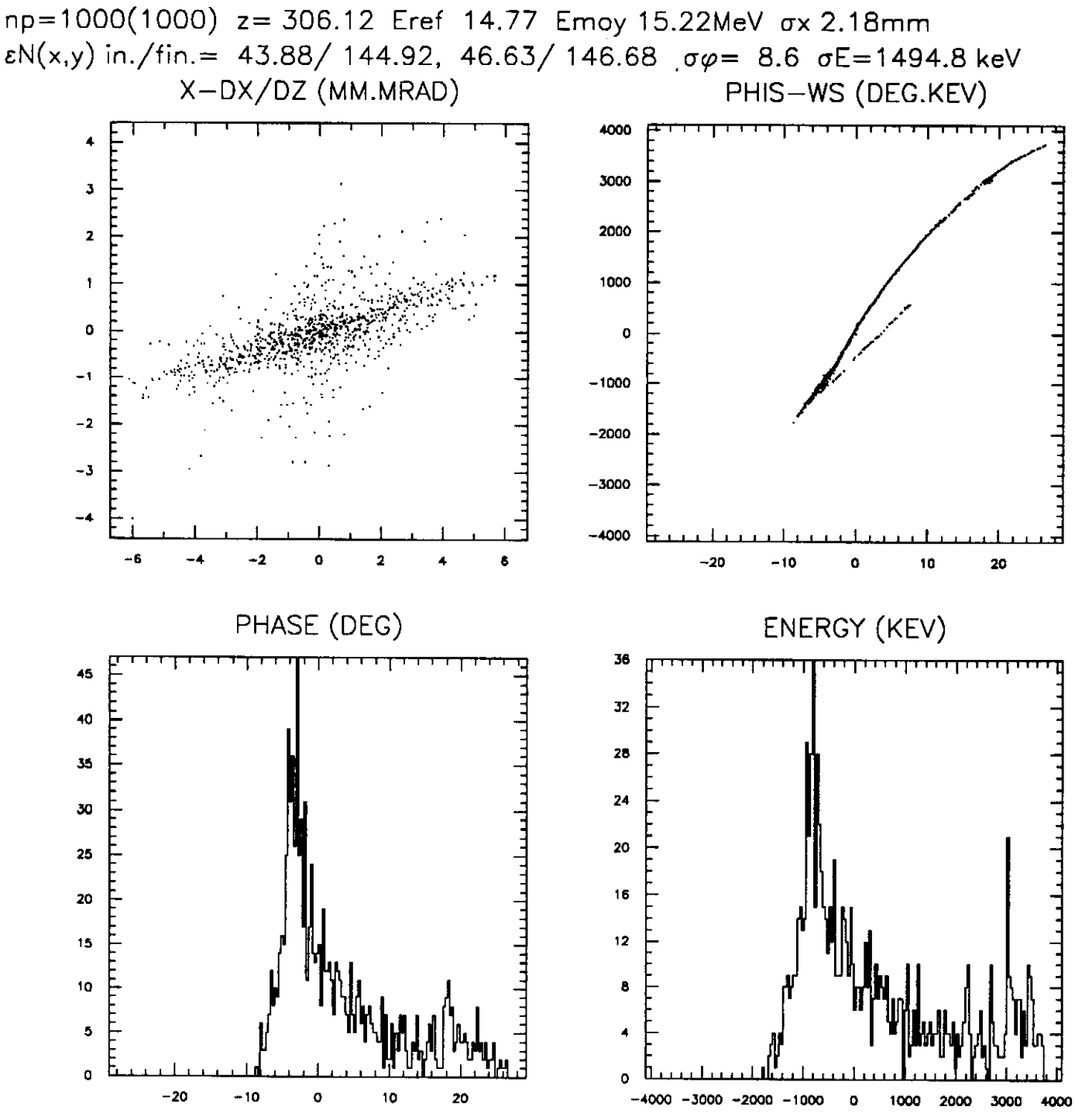

Figure 22: The output at the exit of the 9-cell SC cavity for the first photocathode model.

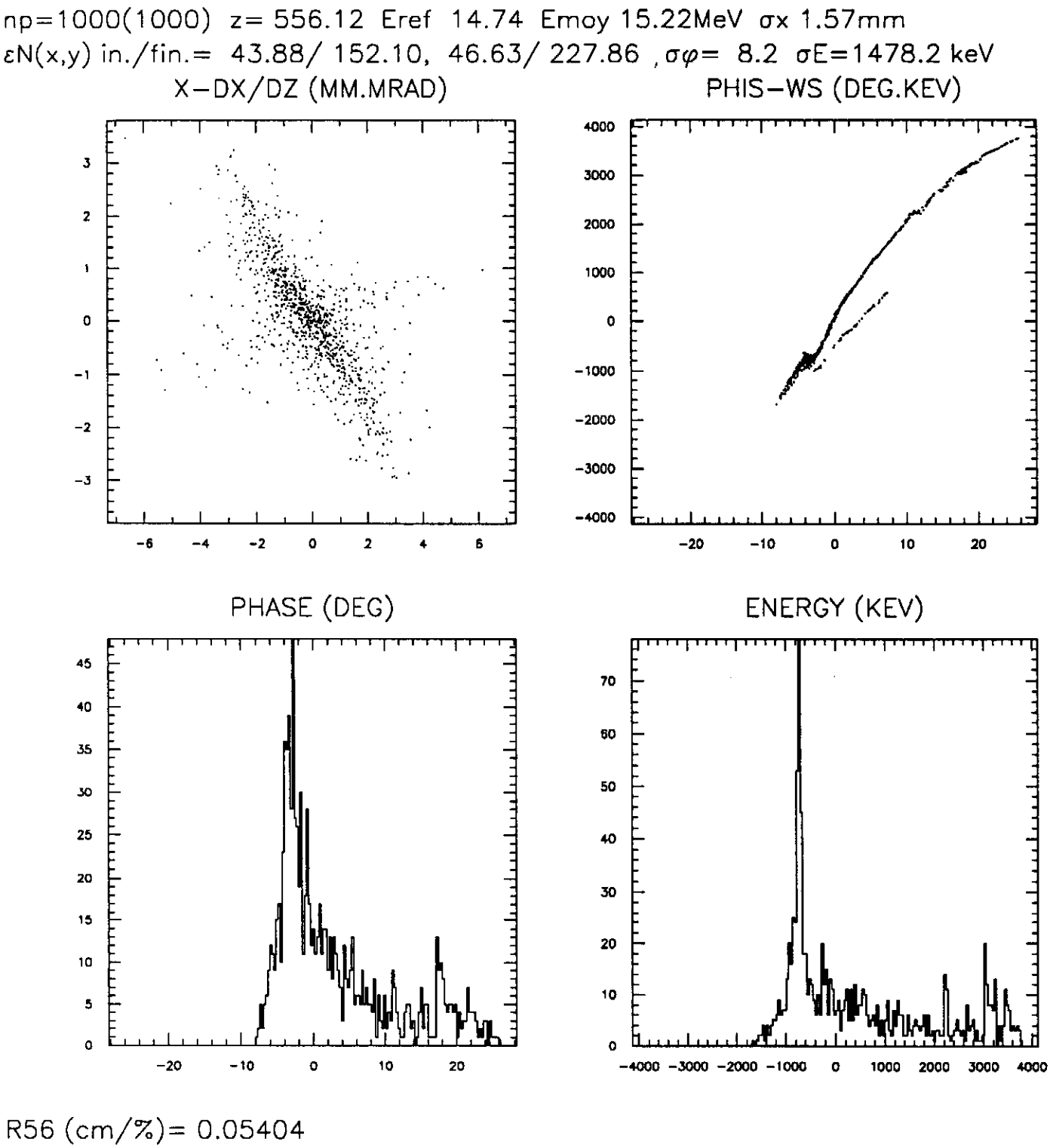

Figure 23: The output at the entrance of the magnetic buncher for the first photocathode model.

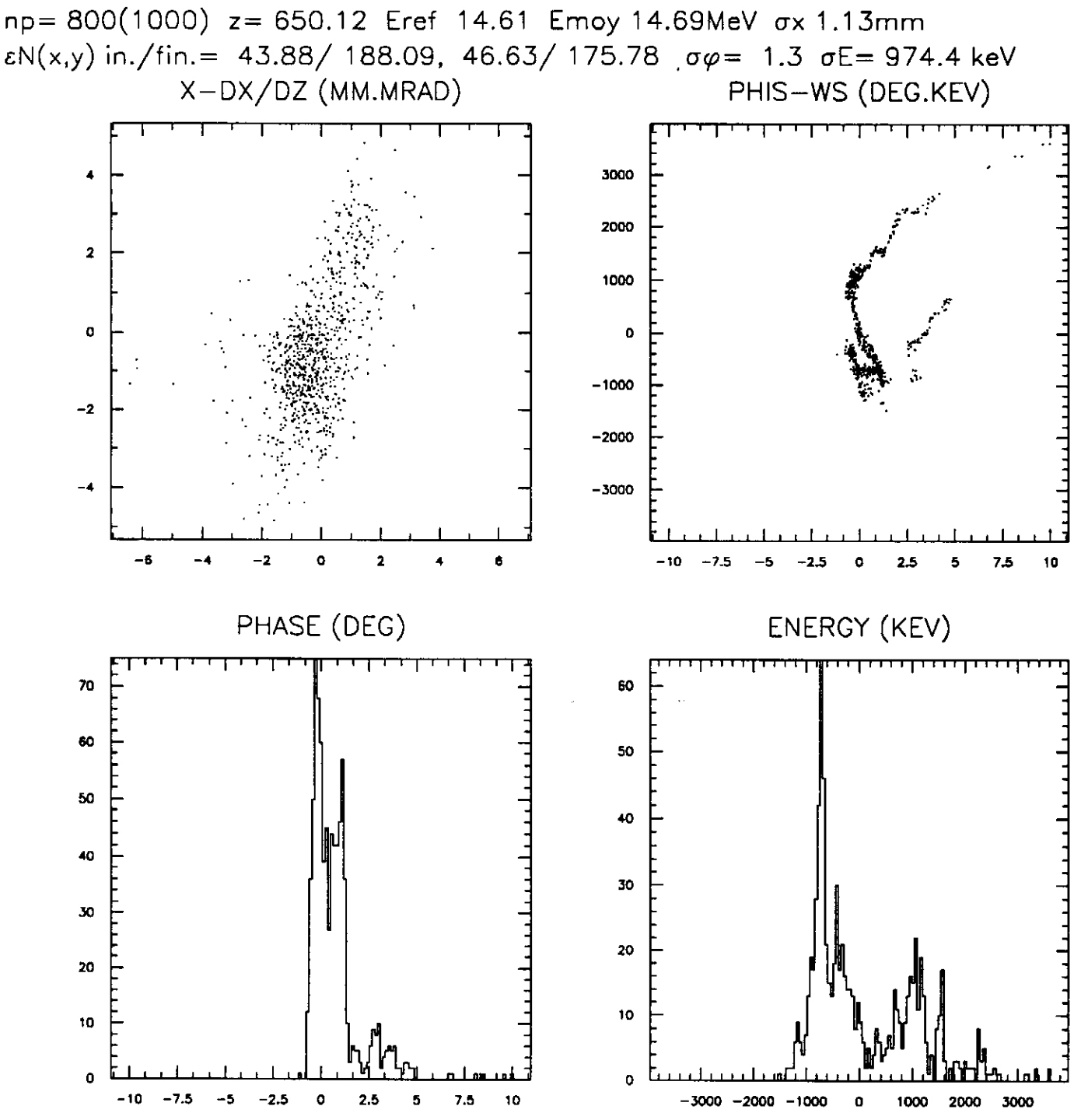

Figure 24: The output at the end of the magnetic buncher for the first photocathode model.

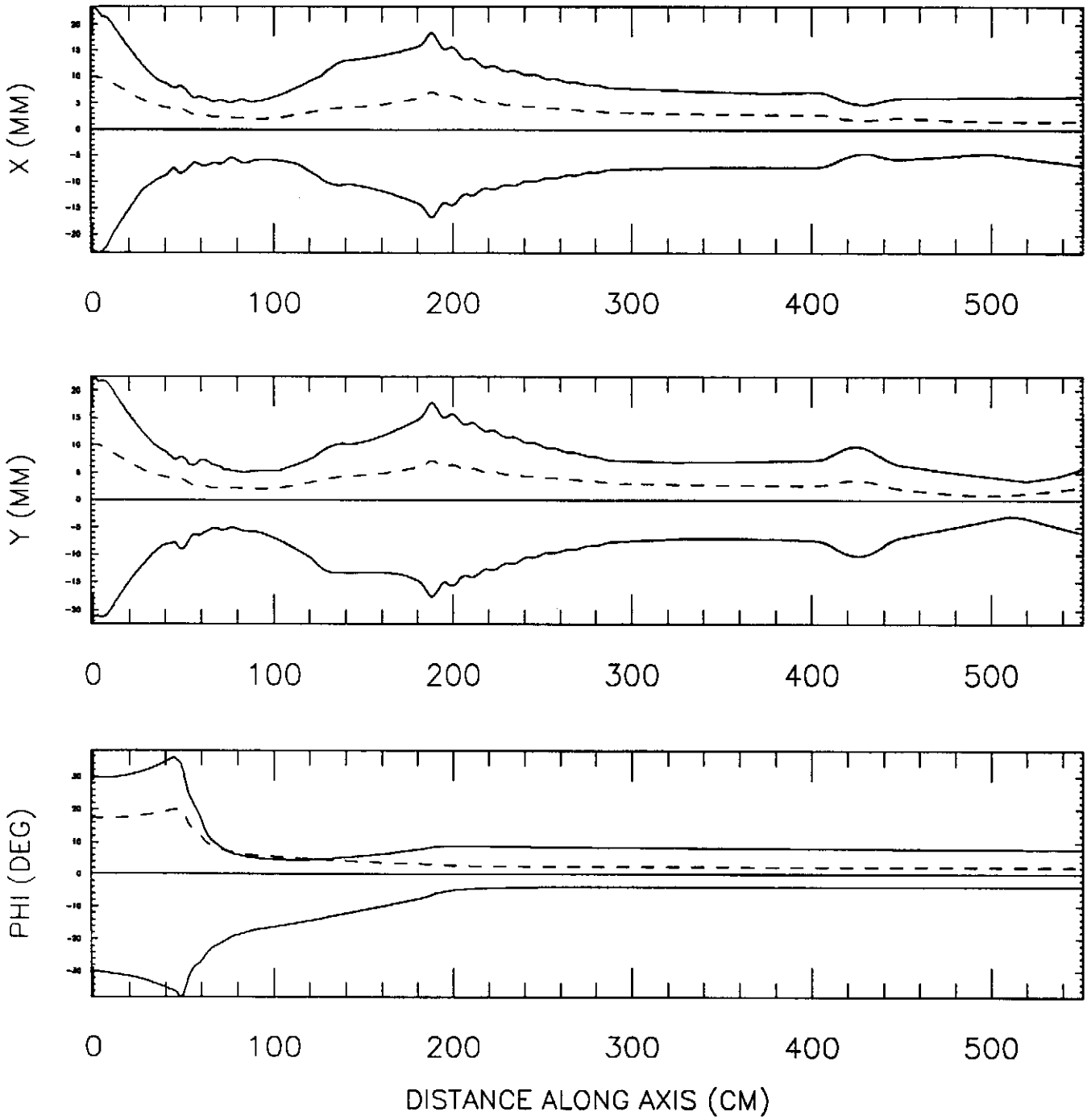

Figure 25: The beam and phase envelopes for the second photocathode model.

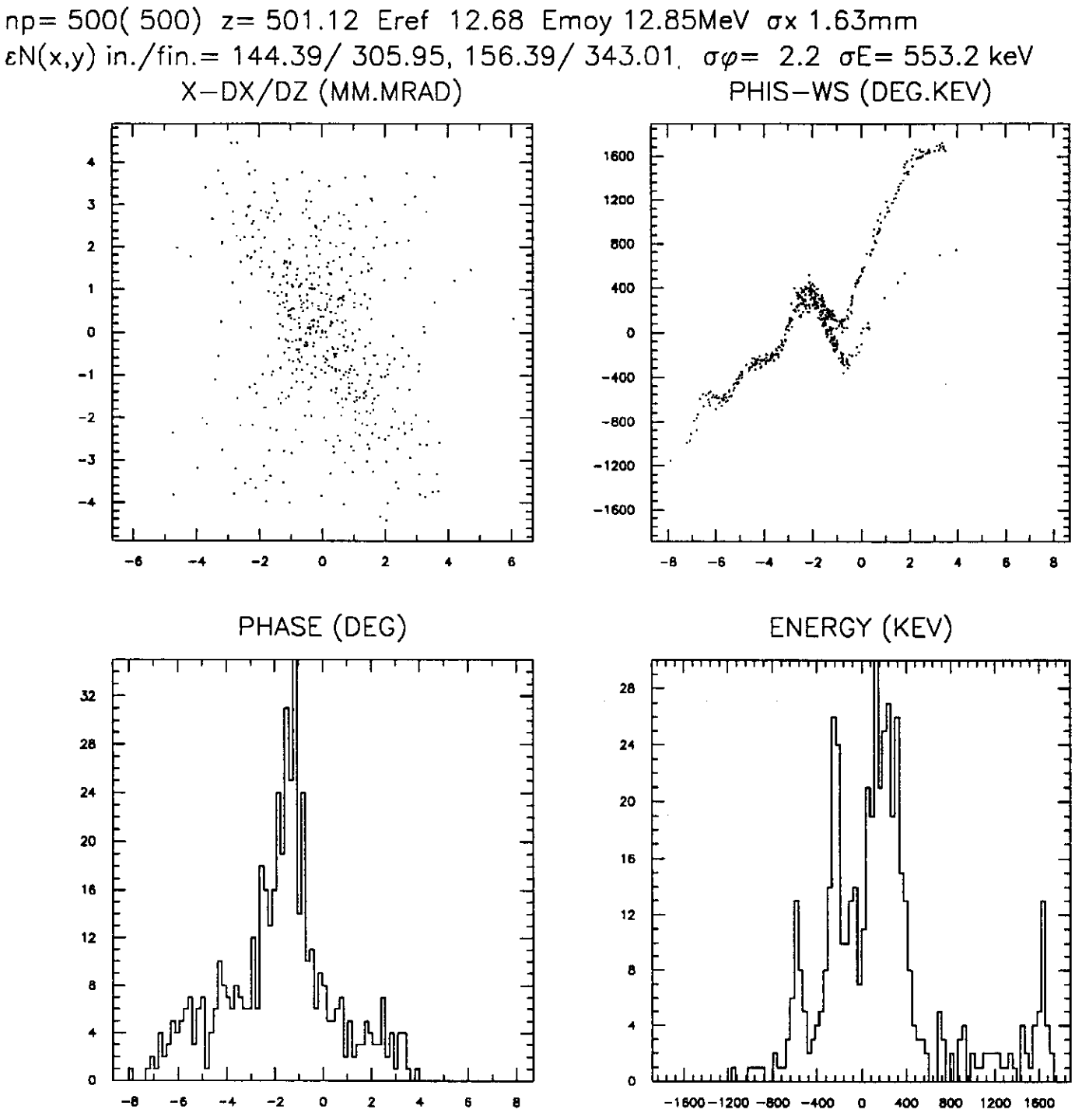

Figure 26: The output at the end of the simulation for the second photocathode model.